The impact of vertical model levels on the prediction of MJO teleconnections. Part I: The tropospheric pathways in the UFS global coupled model

Cheng Zheng[1, 11*], Daniela I.V. Domeisen[2,3], Chaim I. Garfinkel[4], Andrea M. Jenney[5,9], Hyemi Kim[6], Jiabao Wang[7], Zheng Wu[3,10], and Cristiana Stan[8]

[1]Lamont-Doherty Earth Observatory, Columbia University, USA

[2]University of Lausanne, Lausanne, Switzerland

[3]ETH Zürich, Institute for Atmospheric and Climate Science, Zürich, Switzerland

[4]The Fredy and Nadine Hermann Institute of Earth Sciences, Hebrew University of Jerusalem, Israel

[5]Department of Earth System Science, University of California, Irvine, USA

[6]Department of Science Education, Ewha Womans University, Seoul, Republic of Korea

[7]Center for Western Weather and Water Extremes, Scripps Institute of Oceanography, University of California, San Diego, USA

[8]Department of Atmospheric, Oceanic and Earth Sciences, George Mason University, USA

[9]College of Earth, Ocean, and Atmospheric Sciences, Oregon State University, Corvallis, USA

[10]Department of Atmospheric and Environmental Sciences, University at Albany, Albany, USA

[11]School of Marine and Atmospheric Sciences, Stony Brook University, Stony Brook, USA

Manuscript for submission to Climate Dynamics

July 2024

*Corresponding author: Cheng Zheng, cheng.zheng.1@stonybrook.edu

Abstract

This study evaluates the prediction of MJO teleconnections in two versions of the NOAA Unified Forecast System (UFS): prototype 5 (UFS5) and prototype 6 (UFS6). The differences between the two prototypes in the number of vertical layers (64 in UFS5 vs. 127 in UFS6) and the model top (54 km in UFS5 vs. 80 km in UFS6) can potentially impact the prediction of MJO teleconnections. With respect to ERA-Interim, the global teleconnections of the MJO to the Northern Hemisphere show similar biases in 500hPa geopotential height over the North Atlantic and European sectors in both prototypes, whereas UFS6 has slightly smaller biases over the North Pacific region. Both prototypes capture the extratropical cyclone activity occurring in weeks 3-4 over the North Atlantic after the MJO phases 6-7 and over the North Pacific and North America after MJO phases 4-5. Both prototypes successfully forecast the sign and approximate locations of 2-meter temperature anomalies over the mid-to-high latitude continents occurring in weeks 3-4 after MJO phase 3 but fail to capture the sign reversal of anomalies over North America between weeks 3 and 4 after MJO phase 7. Overall, the two prototypes show similar performance in simulating the tropospheric basic state as well as prediction skill of the MJO and MJO teleconnections, suggesting that the increase in model vertical resolution and model top does not strongly improve the prediction of MJO teleconnections in the troposphere in UFS.

Key Words

MJO teleconnections; Subseasonal-to-seasonal forecast; model vertical resolution; UFS.

1. Introduction

The subseasonal-to-seasonal (S2S) time scale (2 weeks to 2 months) defines an intermediate time range between short-term weather (up to 10 days) and climate variations. S2S forecasting plays a critical role in various socio-economic sectors, including agriculture, water management, energy, public health, and disaster preparedness (White et al, 2022). By providing information on potential shifts in weather patterns (e.g., blocking, midlatitude baroclinic waves), extreme events (e.g., heat waves, heavy rain), and climate anomalies (e.g., North Atlantic Oscillation, Pacific North American pattern), S2S forecasts help decision makers, planners, and stakeholders make informed choices (Mariotti et al. 2020).

One of the primary sources of predictability on S2S timescales comes from atmospheric variability patterns, such as the Madden-Julian Oscillation (MJO; Xie et al. 1963; Madden and Julian 1971, 1972). The MJO is a large-scale phenomenon in the tropics that persists for several weeks and exerts a significant influence on weather patterns in the extratropics via atmospheric teleconnections (Matthews et al. 2004; Ferranti et al. 1990; Mori and Watanabe 2008; and Seo and Lee 2017; Stan et al. 2017). This tropical phenomenon is characterized by a pattern of enhanced and suppressed convection that moves eastward along the equator. The MJO teleconnections affect the extratropics via two pathways: i) a tropospheric Rossby wave train and ii) stratosphere-troposphere coupling (Schwartz and Garfinkel 2017; Jiang et al. 2017; Barnes et al. 2019).

As S2S forecast models have been upgraded, the prediction of MJO teleconnections has improved (Stan et al. 2022). Some of the upgrades include the use of new observational datasets and/or data assimilation techniques, technical model developments (e.g., improved physics parameterizations, increased complexity), and increased computational power (e.g., allowing

more ensemble members and higher resolution simulations). In spite of this progress, MJO teleconnections remain challenging to predict in S2S models, and it is unclear what types of model improvements would benefit these predictions the most. One of these potential improvements for the representation of teleconnections is related to the choice of the number of levels used for vertical discretization, vertical resolution in the stratosphere, and/or the location of the model top (Charlton-Perez et al. 2013, Butler et al. 2016; Cai et al. 2017, Schwartz and Garfinkel 2020, Feng et al. 2021, Stan et al. 2022). In the literature, the definition of low versus high top models varies across studies. For instance, Charlton-Perez et al. (2013) categorize models in the fifth Coupled Model Intercomparison Project (CMIP5) as high-top if they have a model top above the stratopause and relatively fine stratospheric vertical resolution, and as low-top if their model top is below the stratopause. Based on these criteria, models with fewer than 40 levels and a top around 1hPa are characterized as low-top models. For evaluating the representation of the stratosphere in subseasonal prediction models, Domeisen et al. (2020a) classified high-top models as models with a top model level above 0.1hPa and several levels above 1hPa. High-top models under such definition allows for resolving wave-mean flow interactions in the lowermost mesosphere in which stratospheric vortex perturbations often originate (Chandran et al. 2014).

Vitart (2017) suggests that S2S models with higher horizontal resolution have a better MJO teleconnection in the troposphere. Richter et al. (2020) show that an increase in vertical resolution in the stratosphere does not improve the prediction of the MJO. However, how vertical resolution impacts the MJO teleconnections in forecast models has not been explored in the literature. Here, we examine the prediction of the MJO and its teleconnections to the extratropics through the troposphere only. The prediction of the stratosphere usually benefits from increased

94 vertical resolution (e.g., Son et al. 2020; Domeisen et al. 2019; Wicker et al. 2023), which may in
95 turn improve the prediction of the troposphere via downward coupling (e.g., Domeisen et al.
96 2020b). Thus, we devote a later, companion paper to the stratospheric pathway (hereafter Part
97 II). In addition to an evaluation of the pattern and amplitude of teleconnections in the large-scale
98 circulation, we examine the extratropical cyclone activity, surface air temperature, and
99 precipitation over the Northern Hemisphere (NH). Because model biases can have an impact on
100 the prediction of MJO teleconnections (Wang et al. 2020b; Zhou et al. 2020; Zheng and Chang
101 2020; Vitart et al. 2022; Garfinkel et al. 2022; Lawrence et al. 2022), an evaluation of mean
102 biases is also conducted.

103 The MJO associated convective anomalies, which act as diabatic heating sources, induce
104 Rossby waves that propagate in the extratropics. The MJO teleconnections are driven by these
105 Rossby waves and associated processes (e.g., Matthews et al. 2004; Riddle et al. 2013; Seo and
106 Son 2012). These Rossby waves may be modulated by the MJO associated diabatic heating (e.g.
107 Seo and Son 2012, Seo and Lee 2017, Zheng and Chang 2019), the extratropical basic state,
108 particularly the extratropical jet stream which influences the propagation characteristics (Wang
109 et al. 2020b; Zhou et al. 2020; Zheng and Chang 2020; Vitart et al. 2022), as well as moist
110 processes in the extratropics which influence wave formation (Pfahl et al. 2015). To understand
111 how the distribution of vertical levels in the atmospheric model influences the prediction of MJO
112 teleconnections, we will assess each of these processes as well as the prediction skill of the MJO
113 (tropical diabatic heating).

114 In this study, we examine the impacts that the distribution of vertical levels in the
115 atmospheric model and the location of the model top have on the prediction of MJO
116 teleconnections in the UFS global coupled model. The Unified Forecast System (UFS) global

coupled model (Stefanova et al. 2022) is the newest generation of the S2S operational forecasting system from the National Oceanographic and Atmospheric Administration. The development of UFS consists of a sequence of 8 Prototypes with incremental upgrades. An increase in the number of vertical levels and model top was included in the upgrade from Prototype (i.e., version) 5 to Prototype 6.

The remainder of this paper is organized as follows: In section 2, we describe the models and observations that are used in this study; results from the simulations are compared with observations in section 3; and we conclude with a summary and discussion of the results in section 4.

2. Data and models

a. Forecast Models

Reforecasts from two versions of the UFS Coupled Model, Prototype 5 and 6 (UFS5 and UFS6), developed by the National Centers for Environmental Prediction (NCEP), are used in this study. The model components of UFS5 and UFS6 are summarized in Table 1. The only difference between these two prototypes is in the atmospheric component of the model. Both prototypes have the same oceanic component (GFDL MOM6 model; Adcroft et al. 2019), sea ice component (Los Alamos CICE6 model) with tripolar 0.25° global grid, and large-scale ocean waves component (WW3DG 2019). In MOM6, the tripolar grid uses 75 hybrid depth-isopycnal coordinates. In CICE6, the tripolar grid is configured with 7 layers for the 5 ice categories and 1 layer for snow. The coupling across the atmosphere, ocean, and sea ice component is achieved via the Community Mediator for the Earth Prediction Systems (CMEPS). The atmospheric component in both prototypes uses the FV3 dynamical core on the cubed-sphere grid (Putman

and Lin 2007; Harris and Lin 2013) at C384 (~0.25°) horizontal resolution and the Common Community Physics Package (CCPP) for physics parameterizations which includes the Noah Land Surface model (LSM). However, the two prototypes have a different distribution and number of vertical layers which increases from 64 in UFS5 to 127 in UFS6. The model top also increases from 54 km in UFS5 to 80 km in UFS6. In Fig. 1, the thickness of each model layer is shown as a function of pressure and compared between the two UFS versions. UFS6 has 11 levels beyond the model top of UFS5. The figure also shows the layer thickness as if UFS5 vertical resolution were doubled (the thickness of each layer is reduced by 50%). Below ~270hPa (the gray line), UFS6 resolution is slightly higher than doubling UFS5 resolution, while above ~270hPa, UFS6 resolution is lower than doubling UFS5 resolution. Note that between 5hPa to 50hPa, UFS6 resolution is much closer to UFS5 resolution than to doubling UFS5 resolution, meaning less increase in the vertical resolution of UFS6. In general, UFS6 vertical resolution is about double compared with UFS5 from the surface to the lower stratosphere (~100hPa). Following the definition in Domeisen et al. (2020a), who compared a wide range of subseasonal forecast models, UFS5 is classified as a low-top model (model top not high enough despite having 64 vertical levels, meaning poor resolution near the stratopause) and UFS6 is classified as a high-top model.

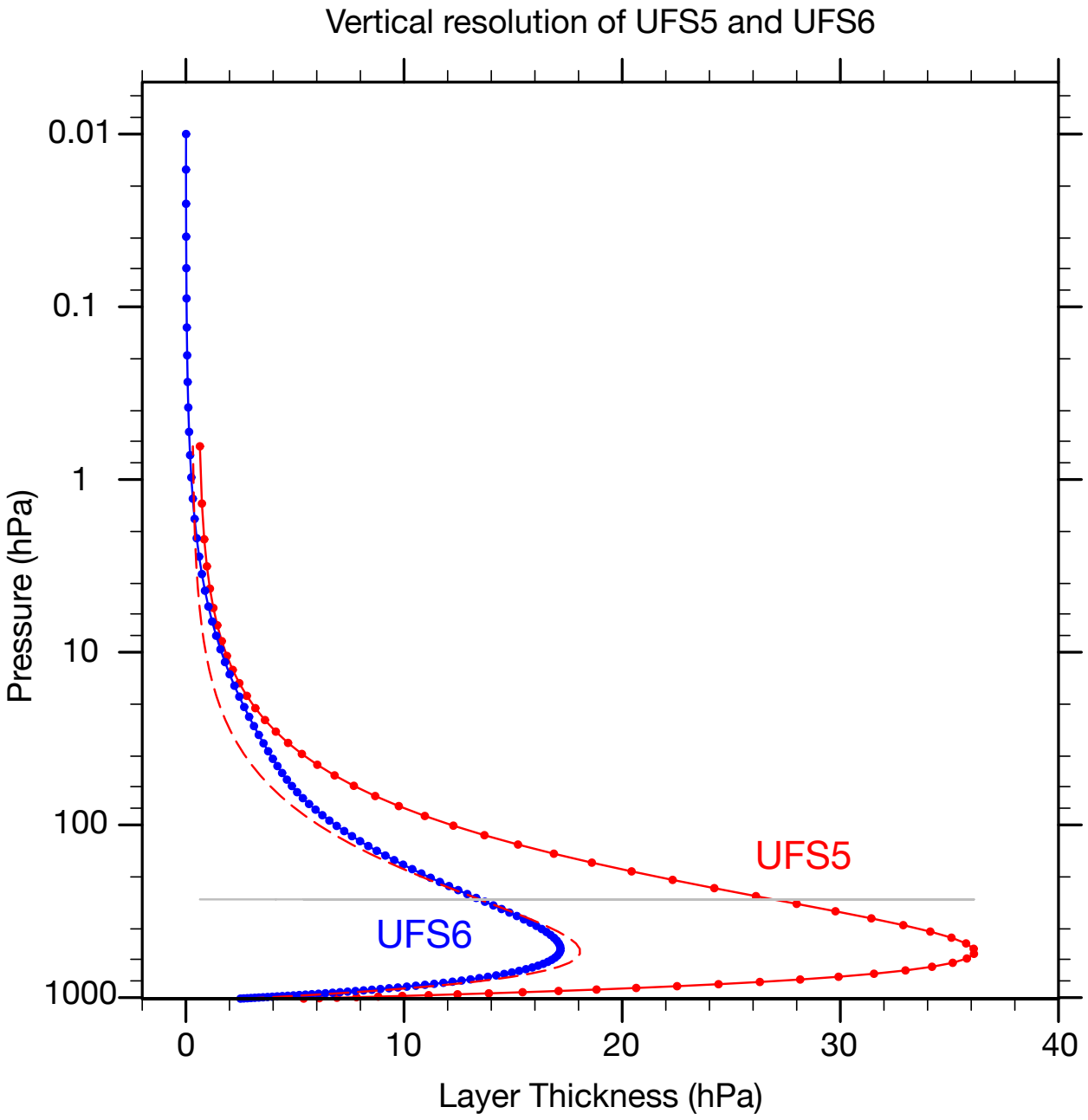

Fig. 1 Vertical resolution of UFS5 (red) and UFS6 (blue). The pressure of each model layer is represented on the y-axis, while the thickness of each layer is represented on the x-axis. The dashed line depicts the distribution as if the thickness of each UFS5 model layer is reduced to its half (doubling UFS5 vertical resolution). The gray line represents the pressure level of 270 hPa.

Prototype	**Atmospheric Model** C384 (~0.25 degree) horizontal resolution			**Ocean Model** Tripolar ~0.25 degree horizontal resolution	**Wave Model** Regular lat/lon 0.5 degree grid	**Ice Model** Tripolar ~0.25 degree horizontal resolution	**Mediator**
	Dynamical Model	**Physics Settings & Driver**	**Land Model**				
UFS5	FV3 64 layers, Non-Fractional grid (model top at 54km)	GFSv15.2, CCPP driver	Noah LSM	MOM6	Wavewatch III	CICE6 (Mushy thermodynamics not turned on)	CMEPS
UFS6	FV3 127 layers, Fractional grid (model top at 80km)	GFSv16, CCPP driver					

Table. 1 Model components of UFS5 and UFS6.

The atmospheric physics package is also upgraded from GFSv15.2 in UFS5 to GFSv16 in UFS6. The upgrades in GFSv16 include: (a) updates in the calculation of the solar radiation absorption by water clouds and cloud overlap assumptions in the Rapid Radiative Transfer Method for General Circulation Models (RRTMG) scheme, which handles shortwave and longwave radiation; (b) updates of the scale-aware hybrid eddy-diffusivity mass-flux (EDMF) scheme (Strobach 2021, 2022) for the planetary boundary layer (National Centers for Environmental Prediction 2019a); (c) addition of a parameterization for sub-grid scale non-stationary waves in the gravity wave drag parameterization scheme; (d) updates in the computation of the ice-cloud effective radius in the microphysics scheme (Zhou et al. 2022); (e)

upgrades in Noah LSM in calculating the heat flux over snow covered surface, and incorporating the vegetation impact on surface energy budget over urban areas. In addition, UFS6 uses fractional grids in the atmospheric component, which allow grid cells along the lake shores and coastlines to be partially covered by land, open water, or sea ice; while in UFS5, each grid cell consists of either 100% land or 100% water. It has been well documented by previous studies (e.g., McTaggart-Cowan et al. 2019; Bauer et al. 2013; E. Lee et al. 2019) that increasing model vertical resolution without changing model physics results in changes in model mean state and possible degradation in prediction skill. Single column experiments in UFS also confirm this point (see Text S1 and Figs. S1-2). Thus, model physics always needs to be tuned or upgraded when model vertical resolution increases, meaning a comparison of numerical prediction models with different vertical resolution is generally accompanied by changes in model physics.

In short, the differences between UFS5 and UFS6 are limited to the atmospheric model component, with UFS6 having doubled vertical resolution and upgraded physics compared to UFS5.

Reforecasts from April 2011 to March 2018 are generated by NCEP for both UFS5 and UFS6. Each reforecast is initialized on the first and fifteenth of each month (168 deterministic reforecasts in total) and forecast lead time extends to 35 days. Both prototypes use the Climate Prediction Center (CPC) Hybrid Global Ocean Data Assimilation System for the ocean model's initial conditions, CPC ice analysis for the sea ice model's initial conditions, and Climate Forecast System version 2 (CFSv2; Saha et al. 2014) for generating the initial conditions of the wave model. Additionally, the atmospheric initial conditions are interpolated from CFSv2 real-time data assimilation. Thus, the two prototypes are initialized in the same way, except that the atmospheric initial conditions provided by CFSv2 are interpolated to different vertical levels (64

198 layers for UFS5 and 127 layers for UFS6). Note that the initial conditions of UFS6, interpolated
199 from CFSv2 assimilation which is on a lower vertical resolution (64 layers) than UFS6, may
200 influence the performance of UFS6.
201
202
203 *b. Data*
204 We compare the reforecasts described above with reanalysis data and observational
205 products. We use surface air temperature (T2m), wind, and geopotential height from the
206 European Centre for Medium-Range Weather Forecasts (ECMWF) interim reanalysis (ERA-
207 Interim, hereafter ERA-I; Dee et al. 2011) at 1.5° horizontal resolution. Note that using ECMWF
208 Reanalysis v5 (ERA5; Hersbach et al. 2020) yields very similar results compared with using
209 ERA-I. We decide to make use of ERA-Interim to be more comparable to a recent assessment of
210 MJO teleconnections in S2S models by Stan et al. (2022). Daily precipitation data for
211 verification is from the Integrated Multi-satellitE Retrievals for GPM (IMERG; Huffman et al.
212 2015), which is provided at a 0.1° horizontal resolution. Outgoing Longwave Radiation (OLR)
213 data is the NOAA Advanced Very High-Resolution Radiometer (Liebmann and Smith 1996)
214 product at 2.5° horizontal resolution. Both observations and reforecast data are regrided to 1.5°
215 horizontal resolution.
216
217 *c. Methods*
218 The methods used for the evaluation of the MJO and MJO teleconnections in the
219 reforecasts have been developed in previous studies and applied to other S2S forecast systems
220 (e.g., Kim et al. 2018, Stan et al. 2022). The focus of the evaluation is on extended boreal winter

(November to March) for which 70 reforecasts in each prototype are initialized during the analysis period. The MJO is defined by the real-time multivariate MJO (RMM) index (Wheeler and Hendon 2004). The RMM index is constructed from the 1st and 2nd principal components of the combined empirical orthogonal functions (EOFs) of 15°N and 15°S averaged OLR, zonal wind at 850hPa and 200hPa. The phases and amplitude of the MJO are calculated with the RMM index following Wheeler and Hendon (2004).

Active MJO events are defined as times when the observed RMM amplitude is larger than one standard deviation at the time when the reforecasts are initialized. There are 48 active MJO initializations in total during the analysis period. Lagged days of RMM phases are defined as days after the reforecast initialization time when the MJO is active in a specific RMM phase at initialization. We evaluate the skill for the RMM index, MJO teleconnections of 500hPa geopotential height (Z500), T2m, precipitation, and extratropical cyclone activity.

Forecast RMM indices are obtained by projecting the predicted OLR and zonal wind anomalies onto the observed eigenvectors following Gottshalck et al. (2010). To evaluate the MJO prediction skill, the bivariate anomaly correlation coefficient (ACC) and root mean-squared error (RMSE) between the predicted and observed RMMs are calculated following Kim et al. (2018).

The climatology of each prototype, which is a function of initialization time and lead time, is defined by averaging the reforecasts that are initialized on the same day of each year (e.g., averaging all reforecasts initialized on January 1 during the period 2011-2018). Then, the anomalies of reforecasts are obtained as the deviation from the prototype's climatology. Reanalysis climatology and anomalies are calculated in the same way during the same time period (2011-2018). For the RMM calculation, the 120-day moving average was removed from

244 the climatology before computing the anomalies. The reforecasts are extended backwards using
245 observations.
246 The Sensitivity To the Remote Influence of Periodic Events (STRIPES) index (Jenney et
247 al. 2019) is applied to evaluate the global MJO teleconnections of Z500 and precipitation in the
248 extratropics. The STRIPES index represents the strength and consistency (across different MJO
249 events) of the MJO teleconnections during the MJO events' life cycles. The index is positively
250 defined and has no upper bound. To obtain the index, lagged composites of atmospheric
251 variables across all MJO phases for a range of lead times are constructed; then the STRIPES
252 index is calculated as the amplitude of the 1-D vector that results from taking diagonal averages
253 of the 2-D matrix of lagged composite anomalies. The propagation of the MJO is considered in
254 the calculation through specification of the slope of the diagonal used in the calculation of the
255 diagonal averages. This slope reflects the MJO's observed propagation rate of roughly 5 to 8
256 days per phase. A larger value of the index represents stronger sensitivity to the MJO influence
257 over a region. More details of the method to calculate the STRIPES index can be found in Jenney
258 et al. (2019).
259 Anomaly correlation can be applied to further evaluate the performance of UFS in
260 predicting the MJO-induced circulation (geopotential height) anomalies in the patterns
261 highlighted by the STRIPES index. Two diagnostic metrics introduced in Wang et al. (2020a) are
262 adopted for this purpose: (a) the pattern correlation coefficient (pattern CC) and (b) the relative
263 amplitude. The pattern CC between the MJO teleconnections of reanalysis and prototypes is
264 calculated over the region where the MJO-associated Z500 anomalies show large variability. The
265 relative amplitude is defined as the Z500 anomaly standard deviation in UFS over the PNA
266 region divided by that in ERA-I.

The model performance in simulating the MJO influence on T2m and extratropical cyclone activity is evaluated by lagged composites of different MJO phases, as well as pattern correlation coefficients of lagged composites between the UFS and ERA-I. The extratropical cyclone activity is represented by the 24-h difference filtered eddy kinetic energy at 850hPa (EKE850) following Yau and Chang (2020),

$$EKE850(t) = \frac{1}{2}\{\overline{[U850(t+24h) - U850(t)]^2} + \overline{[V850(t+24h) - V850(t)]^2}\}$$

Here, the overbar denotes the average during weeks 3-4. U850 and V850 represent the zonal and meridional wind at 850hPa, respectively. The 24-h difference filter, first introduced in Wallace et al. (1988), highlights synoptic-scale variability with periods between 1.2 and 6 days. Many previous studies have shown that the spatial maxima of this 24-h difference filter correspond well with geographical locations where extratropical cyclones exist. The EKE850 obtained from the filtered velocity anomalies represents eddy kinetic energy associated with extratropical cyclones (storm tracks), which is highly correlated with winter precipitation and high wind events (Yau and Chang 2020).

To illustrate how the biases in the jet may influence the MJO-teleconnections, we make use of stationary wave number K_s on Mercator coordinates (Karoly 1983; Hoskins and Ambrizzi 1993):

$$K_s = (\frac{a\beta_M}{\overline{U_M}})^{\frac{1}{2}}$$

where a is the radius of the Earth; $\overline{U_M}$ is the Mercator zonal wind, which is 300-hPa zonal wind divided by the cosine of the latitude. The overbar means a long term average. β_M is the meridional gradient of absolute vorticity on a sphere,

$$\beta_M = \frac{2\Omega cos^2\theta}{a} - \frac{\partial}{\partial y}[\frac{1}{cos^2\theta}\frac{\partial}{\partial y}(\overline{U_M})cos^2\theta]$$

where Ω is the Earth rotation rate, and θ is latitude. Stationary Rossby waves with zonal wave number k are expected to be reflected at or decay beyond the turning latitude, where $K_s = k$. Thus, stationary Rossby waves have to propagate within the region defined by $K_s = k$ and cannot propagate into regions where $K_s < k$. So, the regions with maximum K_s are often referred to as midlatitude waveguides (Hoskins and Ambrizzi 1993). Previous studies have applied this to understand the MJO teleconnection under different background flows (Zheng and Chang 2020; Henderson et al. 2017; Wang et al. 2020b).

The statistical significance of MJO teleconnection composites is assessed using a bootstrap method. For a particular MJO teleconnection composite map, we produce 1,000 similar bootstrap composite maps (samples). Each random bootstrap map consists of the same number of "MJO events" as the original composite, and the "MJO events" are randomly selected in the reforecasts during wintertime regardless of RMM phase or amplitude. The composite value at any grid point of the map is considered statistically significant if it is within the top 2.5% or bottom 2.5% distribution of the 1,000 bootstrap samples.

3. Results

Before investigating MJO teleconnections in the two prototypes, we first evaluate their ability to forecast the tropospheric basic states and the MJO.

a. Model climatology of tropospheric basic state

We use model weekly biases (model climatology minus ERA-I climatology) to evaluate the models' tropospheric basic states; prediction skill is assessed from the RMSE between model anomalies and ERA-I anomalies.

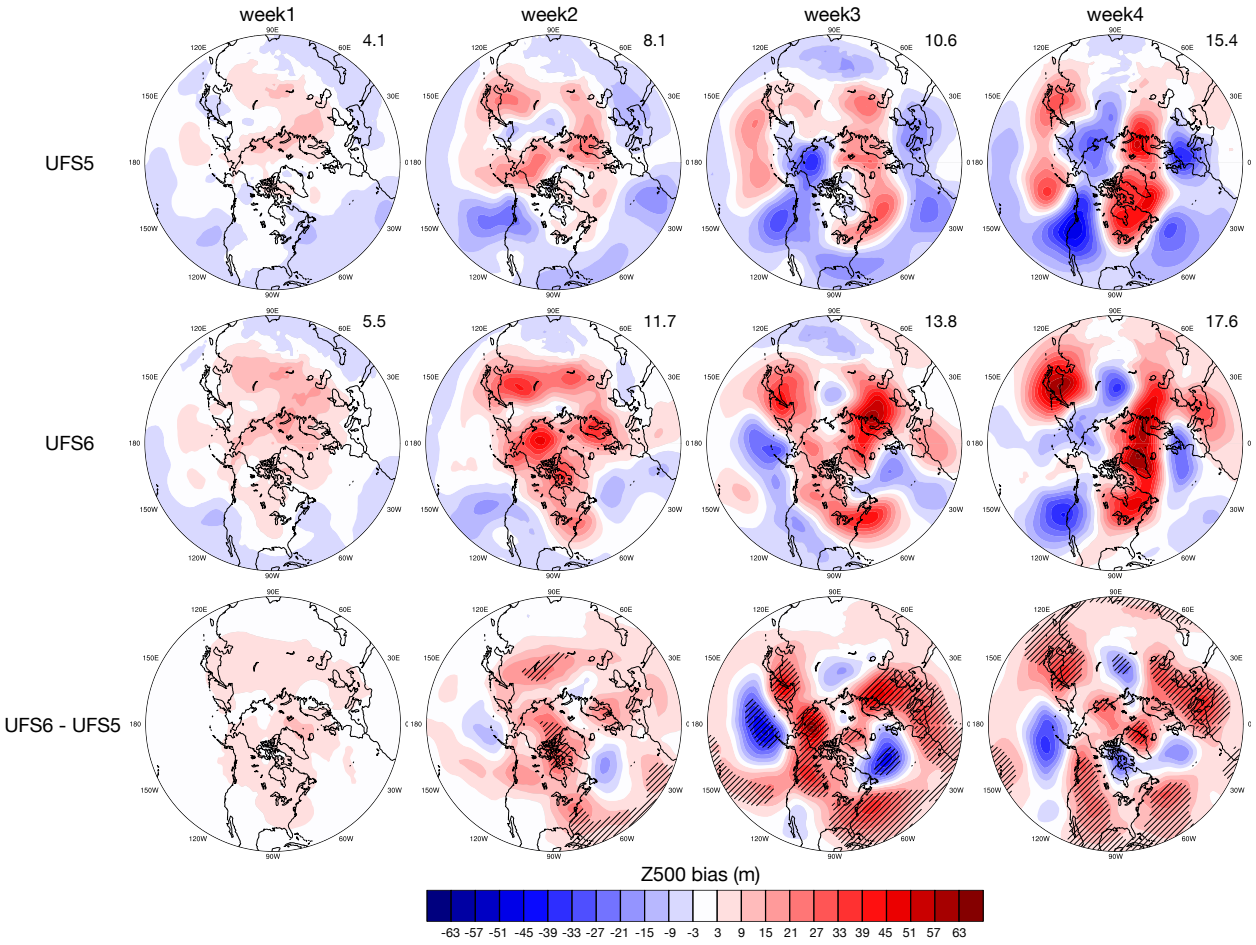

312

313 **Fig. 2** The first two rows show model bias in Z500 during weeks 1 through 4 for UFS5 and

314 UFS6. The numbers at the top-right corner of the bias plots represent area-weighted root mean

315 square bias over the NH. The third row shows the differences between UFS6 and UFS5. Hashing

316 represents regions where differences are statistically significant at the 0.05 level based on a

317 bootstrap resampling calculation.

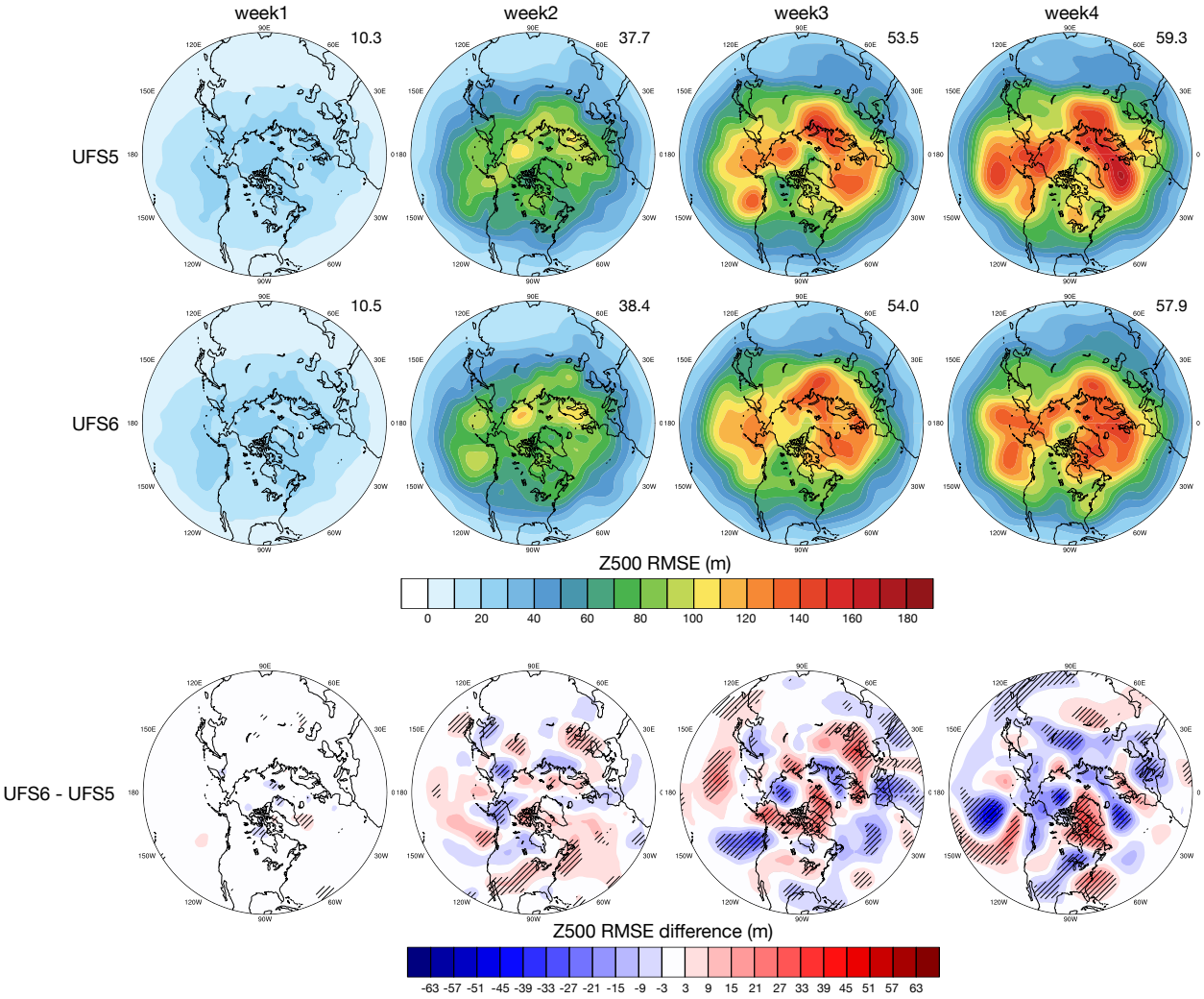

Fig. 3 The first two rows show model RMSE in Z500 during weeks 1 through 4 for UFS5 and UFS6. The numbers at the top-right corner of the bias plots represent area-weighted root mean square RMSE over the NH. The third row shows the differences between UFS6 and UFS5. Hashing represents regions where differences are statistically significant at the 0.05 level based on a bootstrap resampling calculation.

We start with Z500, which represents the large-scale circulation in the extratropics (Fig. 2). The bias in Z500 grows from week 1 to week 4 in both prototypes, which is expected (Straus et al. 2023) as the climatology tends to drift from the initial condition (observed climatology) to

328 the model's own climatology during the simulation. UFS6 has a larger bias over Eurasia but a
329 smaller bias over North America, compared with UFS5. UFS5 has a smaller bias than UFS6
330 when averaged over the NH (shown at the top-right corner of the panels). The spatial patterns of
331 Z500 bias are similar across different weeks within each prototype, suggesting that the increase
332 of model bias is largely due to the error growth in simulating large-scale stationary waves. The
333 spatial patterns of Z500 bias are generally opposite to the climatological stationary waves (not
334 shown), particularly over North America, indicating that both prototypes underestimate the
335 amplitude of stationary waves, which will be further discussed in Part II.
336 The Z500 RMSE in both prototypes also grows from week 1 to week 4 (Fig. 3). UFS5
337 and UFS6 perform similarly in weeks 1-4. Regions with the largest RMSE are over the northern
338 flank of the jet exit over both the North Pacific and the North Atlantic.

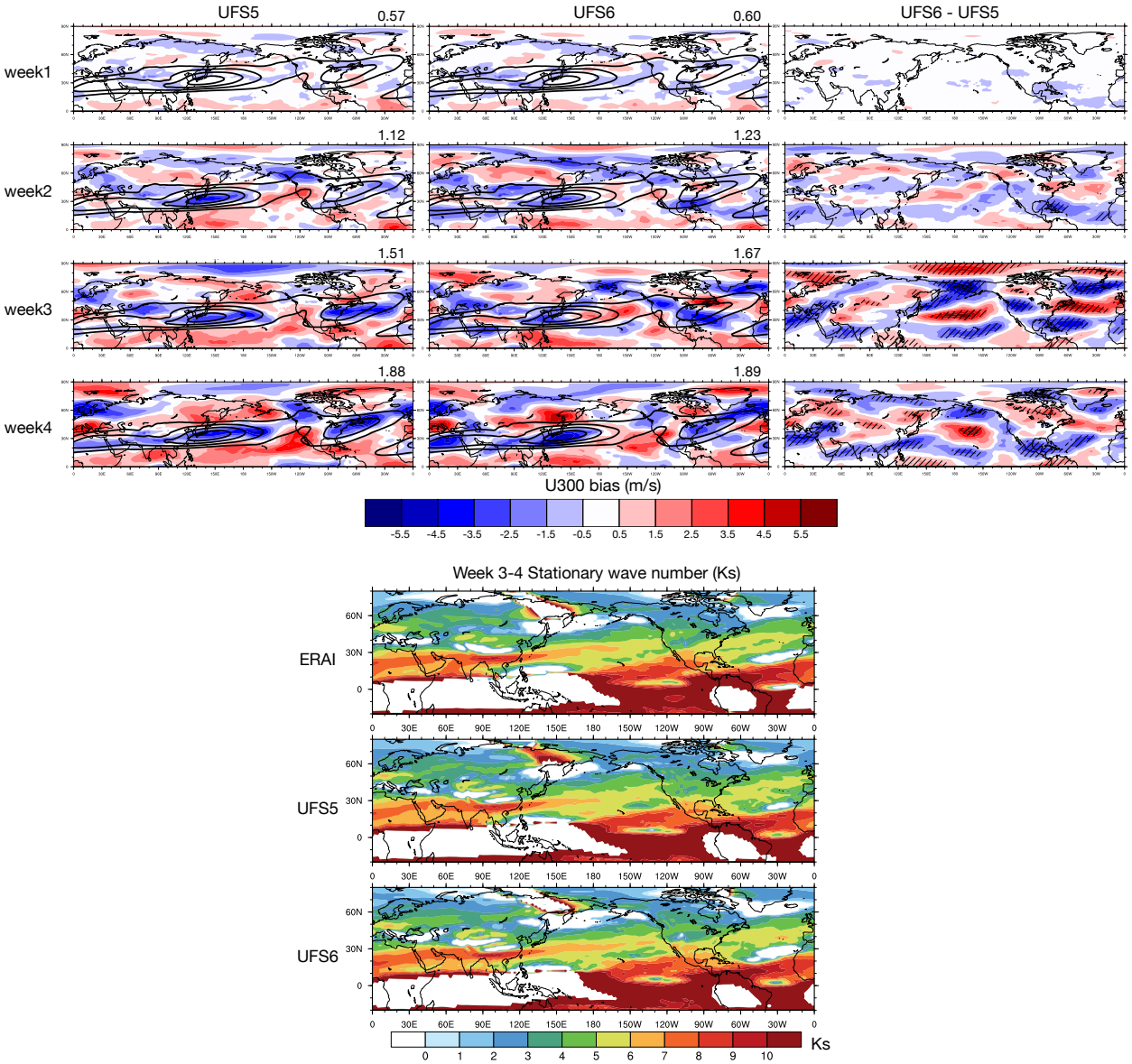

339

340 **Fig. 4** Top panels: Model bias of U300 during weeks 1 through 4 for UFS5 and UFS6. The contours show
341 ERA-I climatology of U300, from 20 m/s to 60 m/s, with an interval of 10 m/s. The numbers at the top-
342 right corner of the bias plots represent area-weighted root mean square bias over the NH. The third column
343 shows the differences between the UFS5 and UFS6. Hashing represents regions where differences are
344 statistically significant at the 0.05 level based on a bootstrap resampling calculation. Bottom panels:
345 Stationary wave number at 300-hPa in weeks 3-4 for ERAI, UFS5 and UFS6.

346

Next, we assess the extratropical jet stream. As discussed in section 1, previous studies (Wang et al. 2020b; Zhou et al. 2020; Zheng and Chang 2020; Vitart et al. 2022) show the extratropical jet plays an important role in modulating the MJO teleconnection. The biases in 300-hPa zonal wind are shown in Fig. 4. The two prototypes show similar biases from week 1 to 4, as the biases grow. Both prototypes underestimate the magnitude of the jet over the core regions of the North Pacific and North Atlantic jet and overestimate the magnitude of the jet over the flanks of the North Pacific jet.

The stationary wave number K_s during weeks 3-4 is shown in Fig. 4. The biases in zonal wind, which is negative over the jet core and positive over the flanks, lead to weaker waveguides in the two prototypes, especially for UFS5 at the jet exit region over the central and eastern North Pacific. The white region to the north of the North Pacific jet, where K_s does not exist due to negative β_M is also smaller in UFS5. Linear Rossby waves cannot propagate in this region.

Overall, the two prototypes show similar biases in the extratropical jet. The biases in midlatitude waveguides, which significantly modulate the MJO teleconnections and depend on the detailed structure of the jet, are smaller in UFS6 than in UFS5, indicating potential benefits from increased vertical resolution and upgrades in model physics.

Similar to biases of Z500, biases in EKE850 (Fig. 5) also amplify from week 1 to week 4. The two prototypes show different spatial patterns of bias, particularly over the North Pacific. In UFS5, the bias has a north-south dipole pattern, with stronger EKE850 over the northern flank of the North Pacific storm track, and weaker EKE850 over the southern flank. In UFS6, EKE850 is stronger than ERA-I over the entire North Pacific storm track. Both prototypes overestimate the amplitude of the North Atlantic storm track starting from week 3.

369 The RMSE of EKE850 (Fig. 6) has maximum values over the North Pacific and North
370 Atlantic storm track regions, where the climatology of extratropical cyclone activity has the
371 highest values. UFS6 shows larger RMSE in both North Pacific and North Atlantic storm tracks
372 compared with UFS5. The positive biases of EKE850 in UFS6 (Fig. 5) over both the North Pacific
373 and North Atlantic storm tracks mean that UFS6 overestimates the amplitude of storm tracks. This
374 also results in larger weekly variability of the storm track in UFS6 compared with UFS5 (not
375 shown), likely leading to larger RMSE in UFS6.

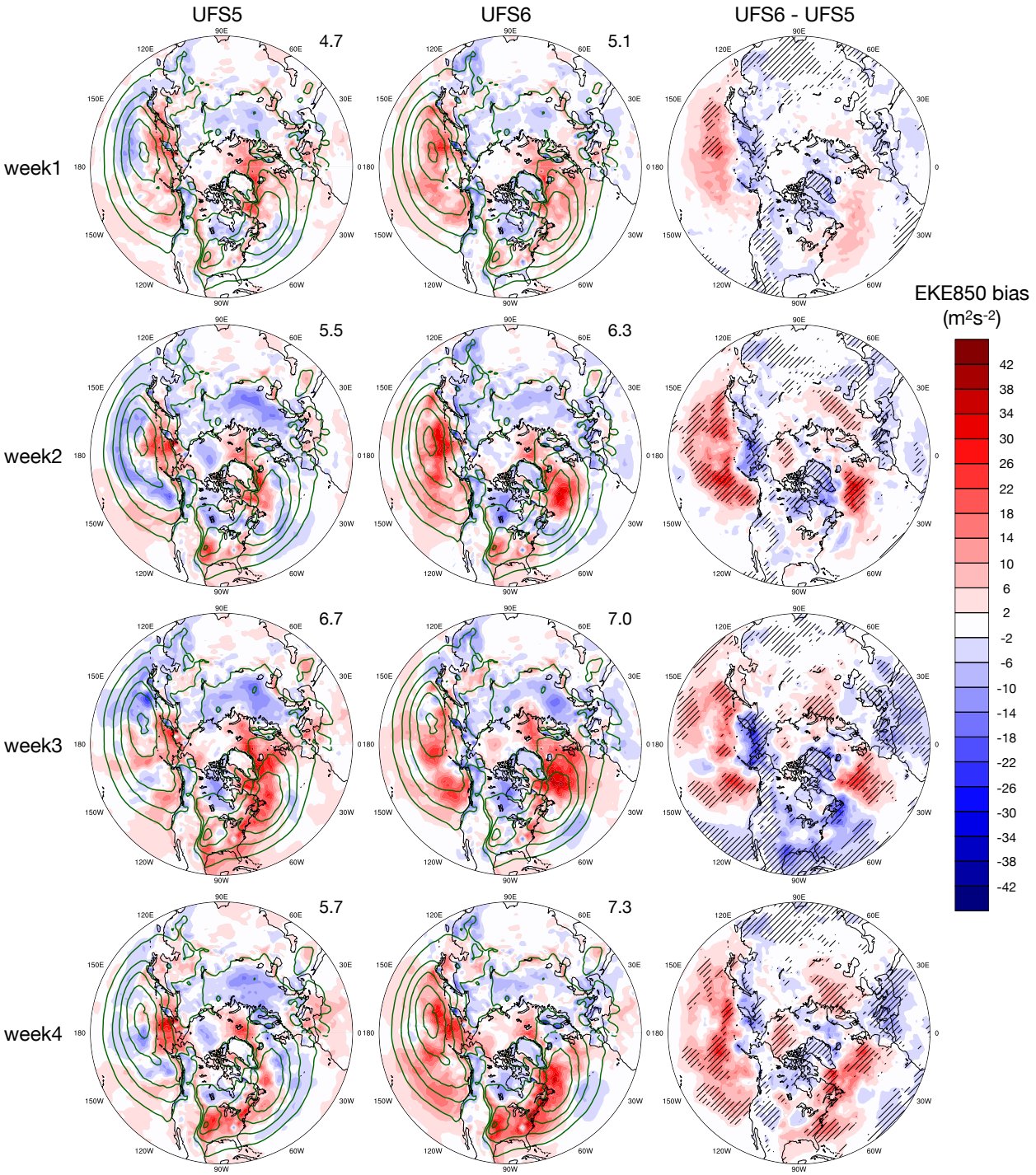

376

377 **Fig. 5** The first two columns: Model bias (shading) and climatology (contours) of extratropical cyclone
378 activity (EKE850). Contour interval is 30 m^2s^{-2}. The numbers at the top-right corner of each panel represent
379 area-weighted root mean square bias over the northern hemisphere. The third column: The differences

between UFS6 and UFS5. Hashing represents regions where differences are statistically significant at the 0.05 level based on a bootstrap resampling calculation.

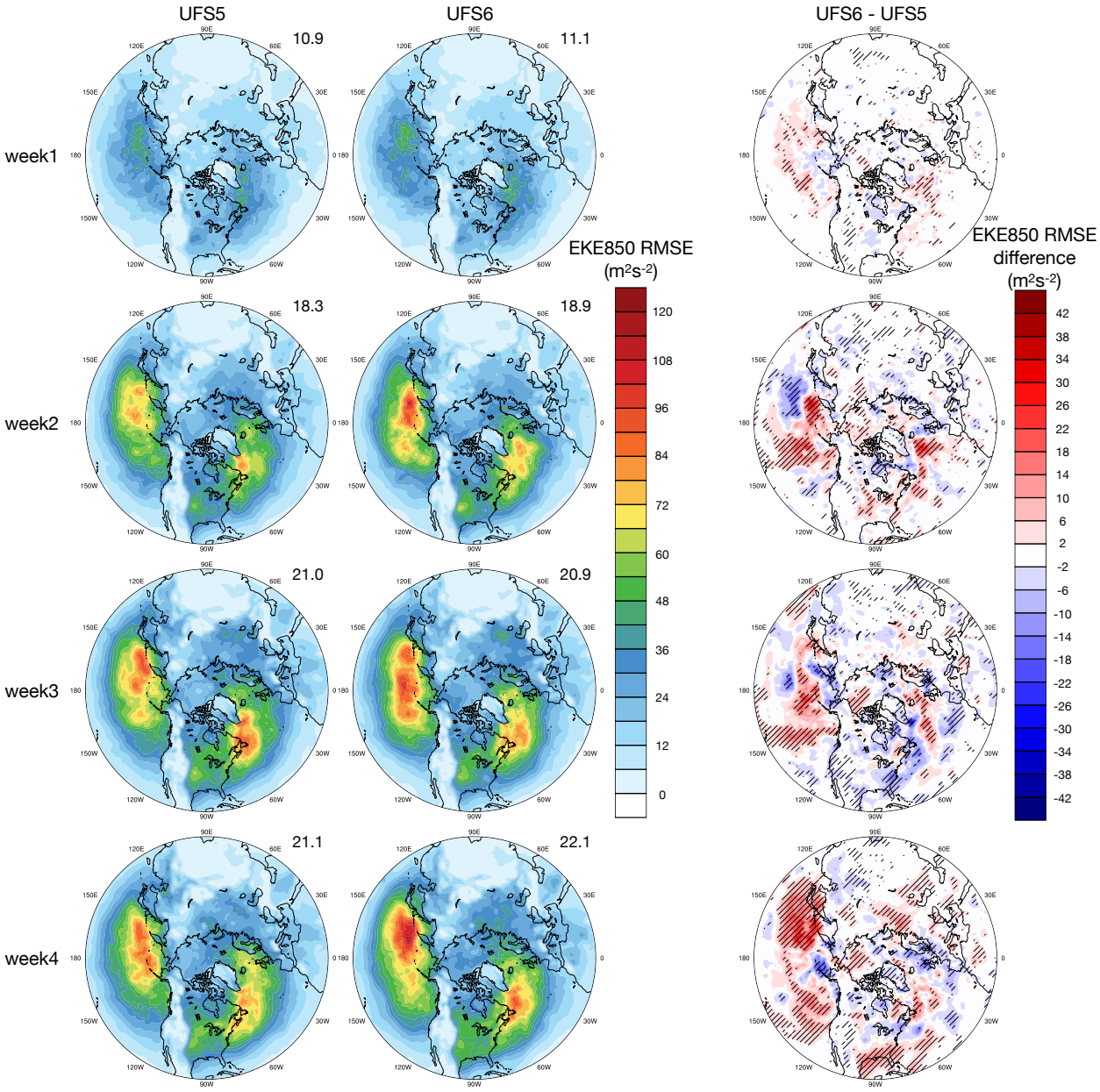

Fig. 6 The first two columns: RMSE of extratropical cyclone activity (EKE850). The numbers at the top-right corner of the RMSE plots represent the area-weighted average of RMSE over the northern hemisphere. The third column: The differences between UFS6 and UFS5. Hashing represents regions where differences are statistically significant at the 0.05 level based on a bootstrap resampling calculation.

In summary, the two prototypes display similar performance in prediction skill as well as simulating the tropospheric basic states. Despite minor improvement in the extratropical waveguides from UFS5 to UFS6, there is no significant improvement in the tropospheric basic states in the extratropics by increasing vertical resolution, which impacts the MJO teleconnection as discussed in section 1. This indicates that higher vertical resolution is not likely to improve MJO teleconnections via improvements in the tropospheric basic state. Prediction skill and model bias in other fields affected by MJO teleconnections such as T2m and precipitation are discussed in Text S2-3 and Fig. S3-6.

b. MJO prediction

The *c*hange in the MJO prediction skill between UFS5 and UFS6 is quantified using the ACC and RMSE metrics. In both prototypes, the ACC continuously decreases and RMSE increases as the forecast lead time increases (Fig. 7). The lead time when models reach an ACC skill of 0.6 is about 16-17 days in both models, while it extends to 23 days in UFS5 and 20 days in UFS6 for an ACC of 0.5. The RMSE increases as forecast lead time increases and the difference between two prototypes is marginal. Bootstrapping tests show no significant differences between the skill of UFS5 and UFS6 at any of the lead days (not shown). Overall, the MJO prediction skill in both prototypes is in the relatively low skill model category when compared with the recent forecasting systems (Kim et al. 2018, 2019). Note that the prediction skill for active MJO cases at reforecast initialization (Fig. 7) and all reforecast cases (not shown) is almost the same.

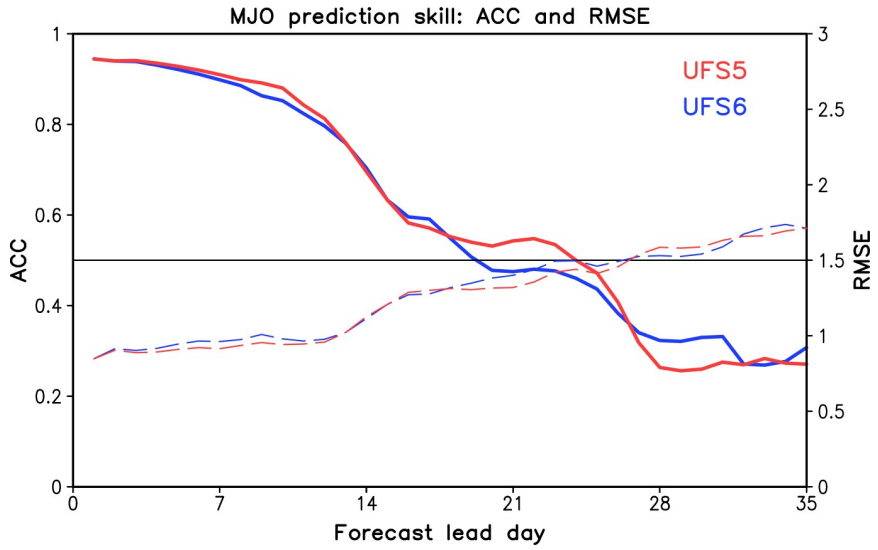

Fig. 7 MJO prediction skill for UFS5 (red) and UFS6 (blue) reforecasts initialized with active MJO events during boreal winter (NDJFM). The prediction skill is evaluated based on the bivariate anomaly correlation coefficient (ACC, solid lines; Rashid et al. 2011) and root-mean squared error (RMSE, dashed lines) between the model and observed RMM indices. Note that the MJO skill evaluation metrics are explained in detail in Kim et al. (2018). The gray solid horizontal line indicates ACC of 0.5 and RMSE of 1.5.

Next, we consider the prediction of eastward propagation of wind and OLR anomalies during strong (active) MJO events over the Indo-Pacific (Fig. 8). We focus on events initialized during phases 2 and 3, when the MJO convective signal is located over the Indian Ocean. Most forecast models predict weaker and slower than observed subsequent propagation across the Maritime Continent, the so-called the Maritime Continent (MC) prediction barrier (Kim et al. 2019). To compare the broad-scale MJO propagation, OLR and zonal wind at U850 anomalies are averaged over 15°S-15°N and displayed as a function of longitude and forecast lead (Fig. 8). While the observed OLR and U850 continue to propagate to the Eastern Pacific, the predicted signals in UFS5 weakens within a week although the U850 signal is somewhat captured until

week 2. In UFS6, while the OLR and U850 signal is stronger than UFS5, the propagation speed is too slow, similar to many of the recent forecast systems (Kim et al. 2019). The MJO propagation speed, roughly estimated by the 0.3m/s 850-hPa zonal wind contour moving from 90°E to 120°E, is about 27 km/hr in observation, 10 km/hr in UFS5, and 9.2 km/hr in UFS6. Note that this noisy signal is largely attributed to the small sample size used for averaging (16 events for phases 2 and 3).

The biases in MJO propagation in both UFS5 and UFS6 lead to similar biases in upper level divergence in the tropics and subtropics (velocity potential in Fig. S8), which has been found to be the key factor to drive the MJO teleconnection in the extratropics (e.g., Henderson et al. 2017; Zheng and Chang 2020; Wang et al. 2020b). Similar biases can be found in the phases 6-7 composites (Fig. S7 and S9).

The increase in vertical resolution and upgrades in model physics do not show clear improvements in predicting the MJO, consistent with Richter et al. (2020). From the results above, increasing vertical resolution in UFS does not show significant benefits in predicting the MJO and the tropospheric basic states (section 3a), which are the two major factors modulating the prediction of the MJO teleconnection as discussed in section 1. This suggests that the increase in vertical resolution may not improve the MJO teleconnection in the troposphere much. We will test this hypothesis and analyze whether there are improvements in the MJO teleconnection due to increased vertical resolution in the following subsections in section 3.

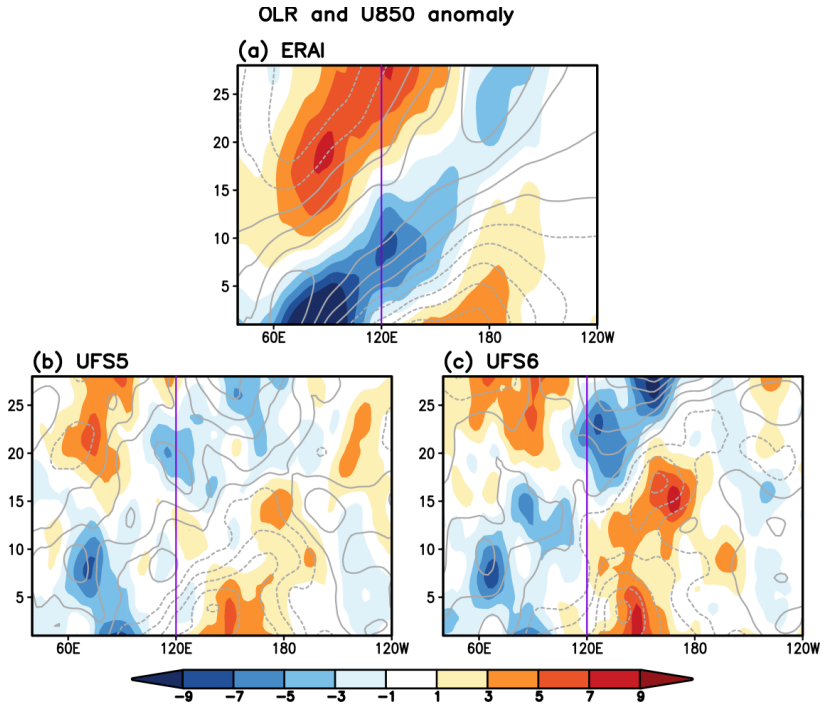

Fig. 8 Longitude-time composites of OLR (W/m2; shading) and U850 (contour; interval 0.3 m/s) anomalies averaged over 15°S-15°N for active MJO events starting from day 1 of the reforecasts initialized in the MJO phases 2 and 3. The vertical lines indicate 120ºE (approximately the center of the Maritime Continent), respectively. A 5-day moving average is applied.

c. MJO teleconnections to the Northern Hemisphere geopotential height distribution

We first evaluate week 1 through 4 forecasts of the Z500 teleconnection following active MJO events in phases 2-3 and 6-7 at initialization. The Z500 composites over the Northern Hemisphere are shown in Fig. 9 (the MJO phases 2-3) and Fig. 10 (the MJO phases 6-7). Since PNA-like patterns of MJO-teleconnection are noticeable in ERA-I in these MJO phases, we focus on the PNA region (20°–80°N, 120°E–60°W, depicted by the black line). Both UFS5 and UFS6 capture the Z500 teleconnection relatively well during the first two weeks (pattern CC > 0.6), while the weekly pattern CC becomes very small starting from week 3. In general, in UFS6 the pattern CC of MJO teleconnections over the PNA region after the MJO phases 2-3 especially at week 3 to

461 4 is higher than in UFS5. UFS6 performs better than UFS5 in predicting teleconnection patterns
462 related to the MJO phases 6-7 at week 3 and has comparable/slightly lower skill than UFS5 at
463 other lead times. Since UFS6 does not seem to better predict the evolution of the MJO initialized
464 in phases 6-7 (Fig. S7) and the associated upper level divergence (velocity potential at 200-hPa in
465 Fig. S9), the better performance of UFS6 at week 3 likely rises from a better simulation of the
466 extratropical evolution of teleconnections in UFS6. This is also suggested by the extratropical
467 waveguides in Fig. 4 as UFS6 is more similar to ERAI compared to UFS5.

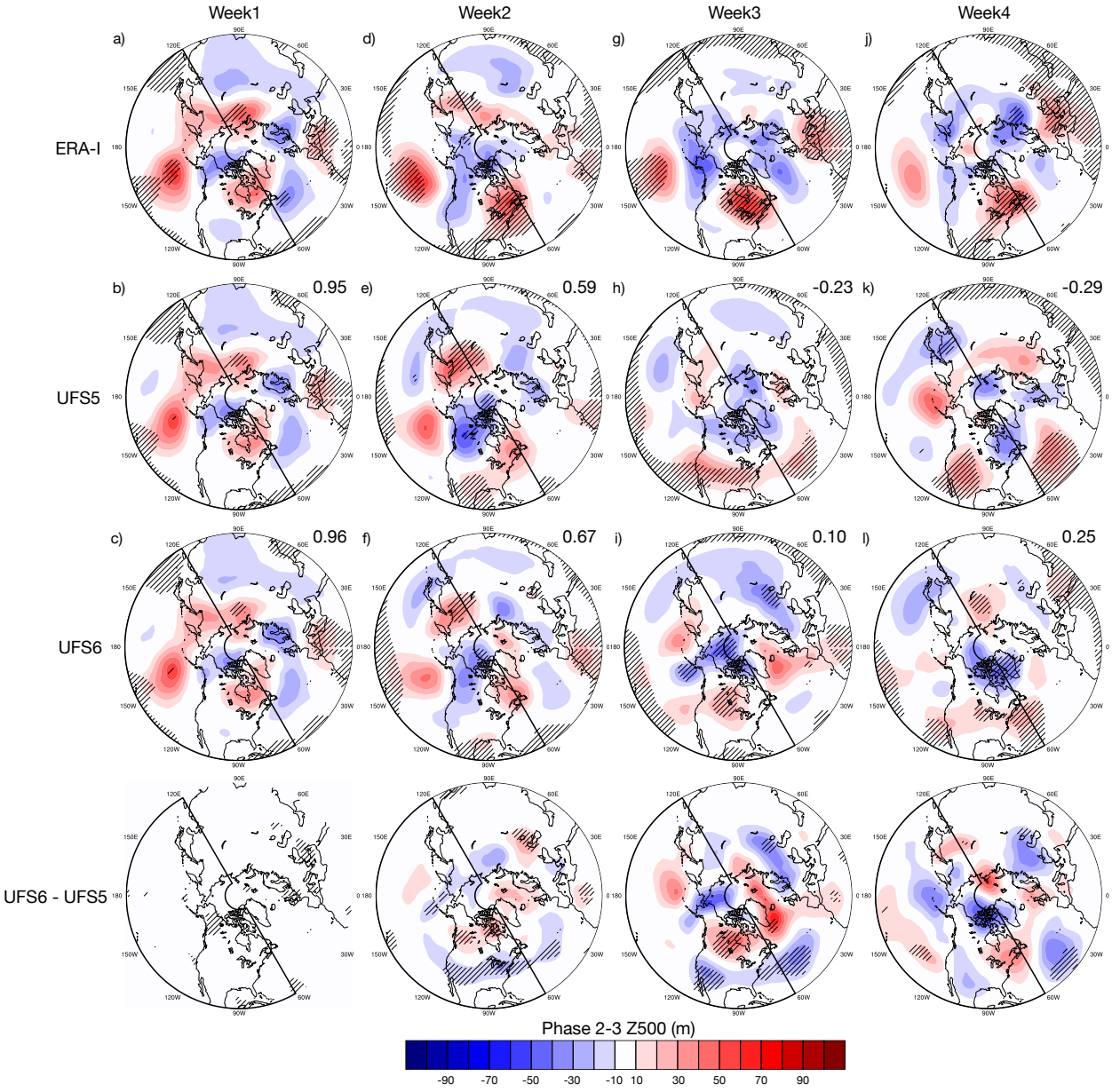

Fig. 9 Composites of the Z500 anomalies (Unit: m) from week 1 to 4 after MJO events in phases 2-3 in the initial condition for ERA-I, UFS5, and UFS6, as well as the differences between UFS5 and UFS6. The black line outlines the Pacific-North America region where the Pattern CC and relative amplitude of MJO Z500 teleconnection are evaluated. Hashing represents regions where the anomalies are statistically significant at the 0.05 level based on a bootstrap resampling calculation. Numbers in the upper right show the pattern CC over the PNA region.

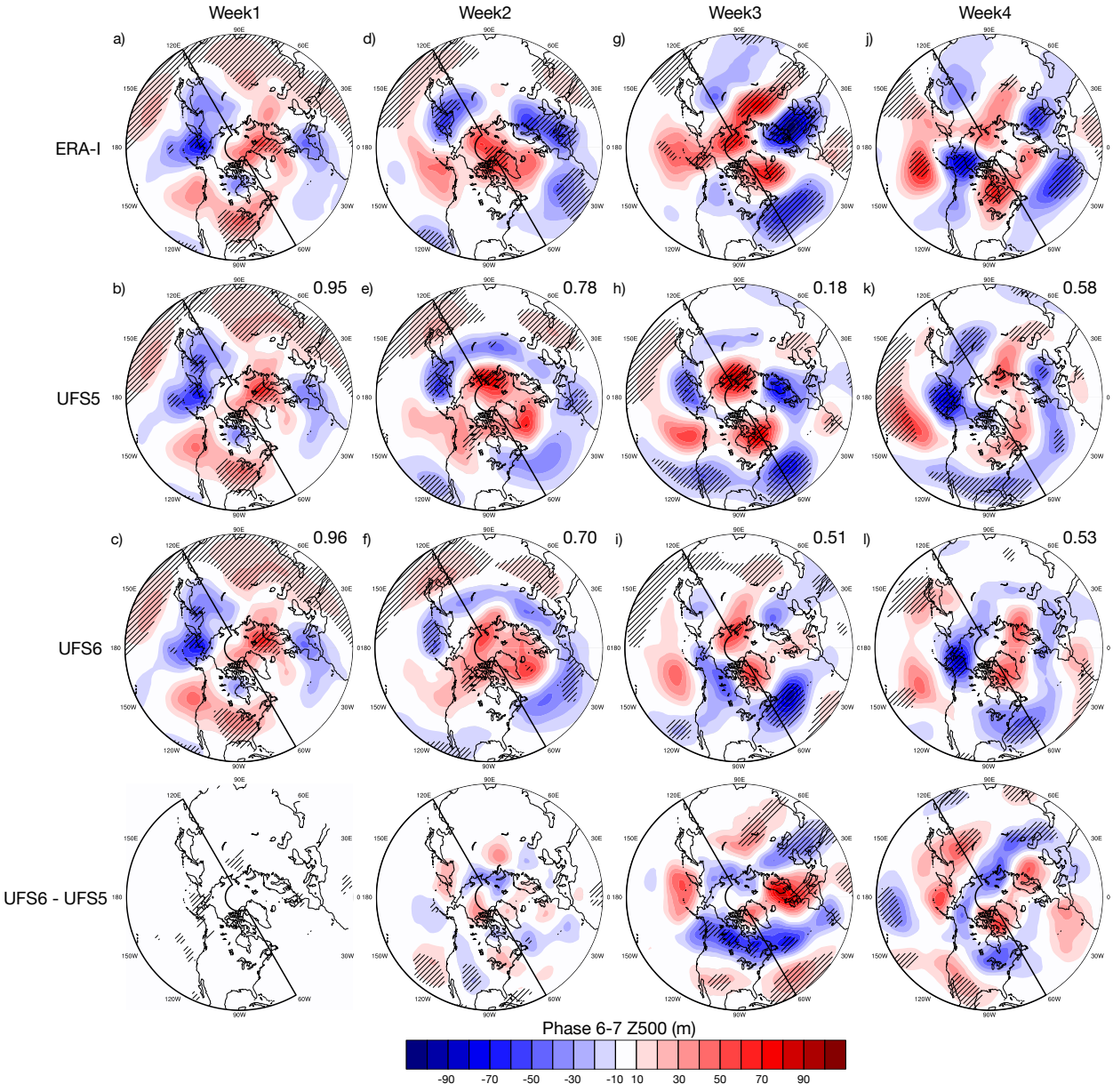

476

477 **Fig. 10** Similar to Fig. 9, but for phases 6-7.

478

479 The average pattern CC of individual reforecasts, instead of pattern CC of the composites
480 (discussed above), is summarized in Fig. 11, which also includes the relative amplitude metric.
481 The decrease of the pattern CC below 0.5 during the second week of the forecast (Fig. 11a-b) is
482 similar to other S2S models (Stan et al. 2022). In weeks 3-4, the amplitude of teleconnections in
483 UFS6 is slightly closer to ERA-I values than in UFS5 for the MJO phases 2-3 (Fig. 11c) and

overestimated for the MJO phases 6-7. Overall, UFS6 performs slightly better in capturing the Z500 teleconnections over the PNA region.

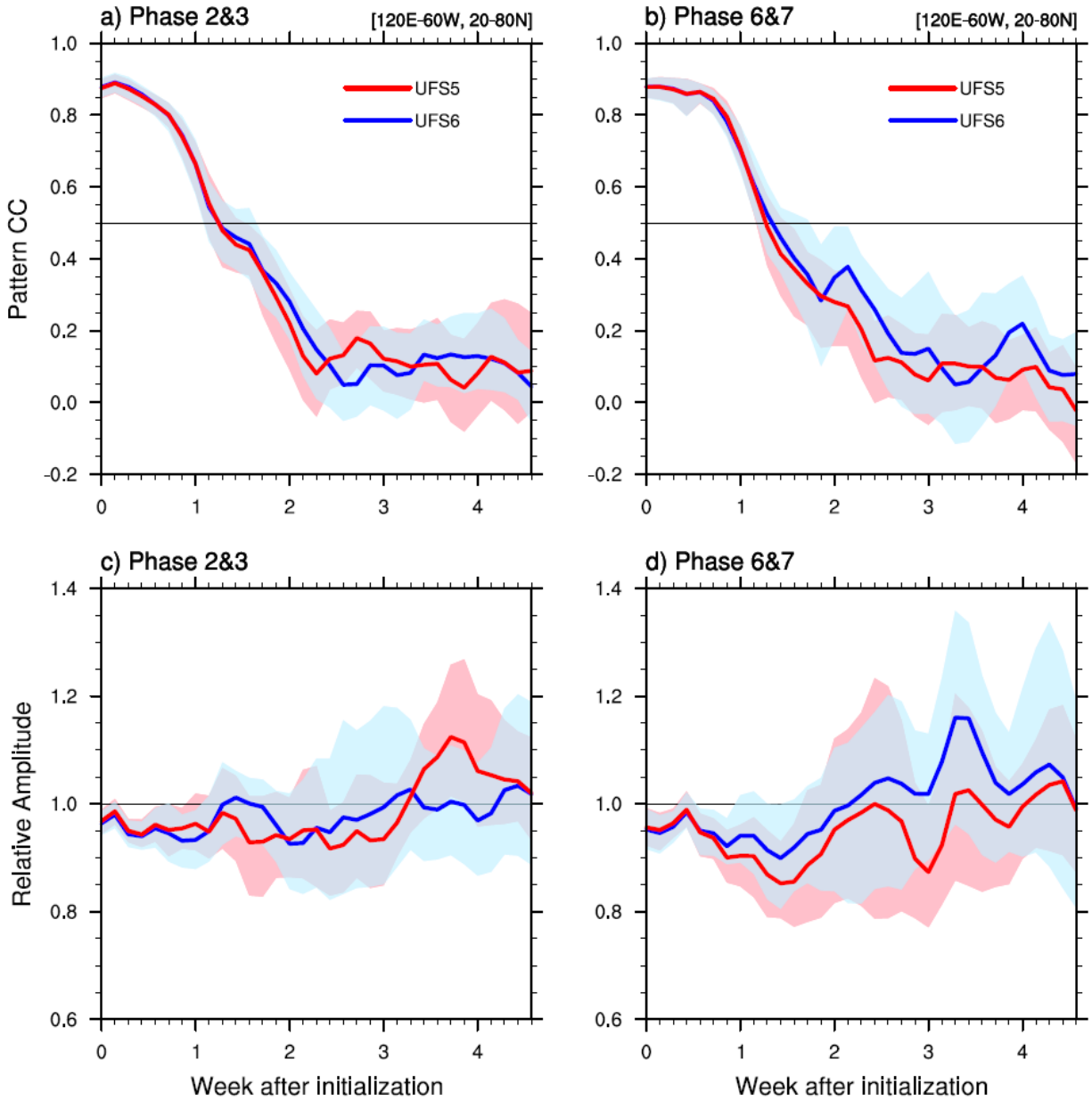

Fig. 11 Pattern correlation coefficient (UFS vs ERA-I) and relative amplitude (UFS/ERA-I) of 500hPa geopotential height anomalies over the PNA region (20°-80°N, 120°E-60°W) vs forecast lead days for the MJO phases (a),(c) 2-3 and (b),(d) 6-7. Horizontal solid lines in (a) and (c) represent the reference line of

pattern correlation at 0.5. Horizontal solid lines in (b) and (d) represent the reference line above (below) which the Z500 anomalies are overestimated (underestimated) in UFS models. The color shadings indicate the 95% confidence intervals for UFS5 (pink) and UFS6 (light blue) determined by the bootstrap test. The lower boundary represents the minimum 2.5th percentile of the bootstrapping distribution between the models, and the upper boundary represents the maximum 97.5th-percentile distribution between the models.

The pattern CC and relative amplitude metrics can be applied to other regions with an a priori known influence of the MJO. The a priori requirement can be a disadvantage and a limitation for revealing potential shifts in the regions of MJO influence in the model or spurious model teleconnections. These limitations can be addressed by applying the STRIPES index.

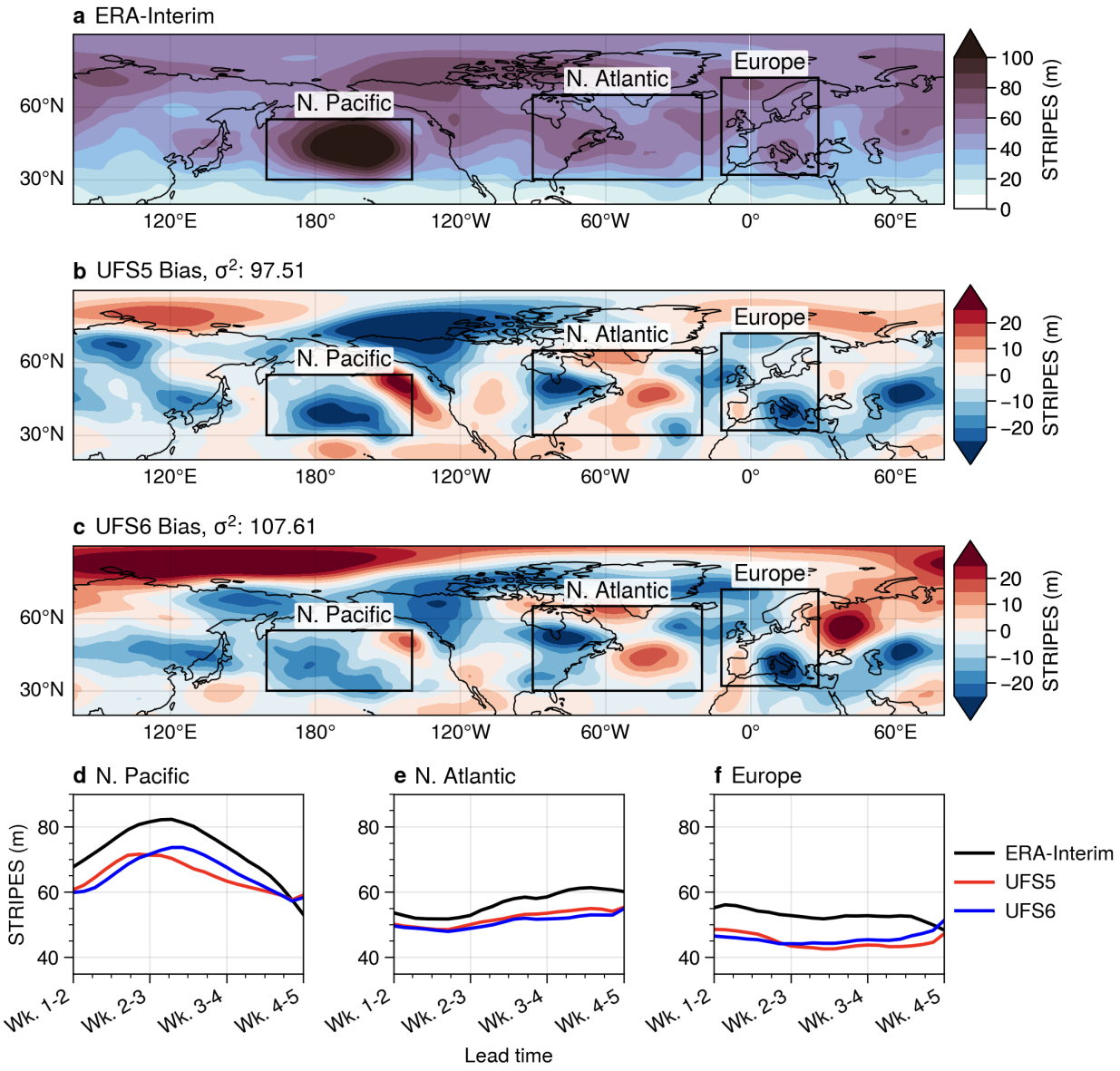

Fig. 12 (a) ERA-I weeks 2-3 extended winter Z500 STRIPES index, and the forecast error in (b) UFS5, and (c) UFS6. For overlapping 2-week windows the ERA-I and forecast STRIPES index for Z500 averaged over the (d) North Pacific (160°-220°E, 30°-55°N), (e) North Atlantic (270°-340° E, 30°-65° N), and (f) Europe (348°-28°E, 32°-72°N). Boxes in panels (a-c) correspond to the regions shown in panels (d-f).

Fig. 12a shows the ERA-I winter STRIPES index for Z500 for weeks 2-3. The North Pacific has the largest value of the STRIPES index, indicating strong co-variability of geopotential

510 height with the MJO there. Larger values are also found throughout the extratropics, with near-
511 zero values in the tropics reflecting the small variability of geopotential height. Fig. 12b-c shows
512 the error in the STRIPES index for UFS5 and UFS6, respectively. Over the North-Pacific and
513 Northwestern North America regions, we see a low-high-low wave pattern in the UFS5 error. This
514 error is reduced by about 10m in UFS6. Nonetheless, the spatial variance of the error over the
515 Northern Hemisphere (20°-90°N) is increased from 97.51 m^2 in UFS5 to 107.61 m^2 in UFS6,
516 which is largely contributed to by much stronger positive errors in UFS6 in Eastern Europe and
517 over the Arctic.

518 Next, we inspect the temporal evolution of the STRIPES index for different regions. Fig.
519 12d-f shows the time series of the STRIPES index from ERA-I, UFS5, and UFS6 computed using
520 overlapping 2-week windows over the North Pacific, North Atlantic, and Europe (see Fig. 12). We
521 note that these are computed using the STRIPES index for each of ERA-Interim, UFS5, and UFS6,
522 which is positive definite (as in Fig. 12a). Over the North Pacific, where the MJO teleconnections
523 are mostly driven by the tropospheric pathway, the STRIPES index for Z500 peaks in weeks 2-3,
524 consistent with the time between Rossby wave excitation and propagation to the region. UFS5 and
525 UFS6 both roughly capture this delayed peak, however UFS5 peaks a few days too early, while
526 UFS6 peaks a few days too late. Both UFS5 and UFS6 also have weaker magnitudes than ERA-I,
527 with UFS6's magnitude improving somewhat from UFS5 in the latter half of the forecast period,
528 while its magnitude worsens in the first third of the forecast period. These findings are consistent
529 with the results of the pattern CC and relative amplitude metrics. Over the North Atlantic, where
530 the MJO teleconnection can be influenced by both the tropospheric and stratospheric pathway, the
531 magnitude of the STRIPES index is smaller, with a delayed peak that occurs between weeks 3-5.
532 Both UFS5 and UFS6 capture this delayed peak, albeit with weaker magnitudes that do not

noticeably improve between UFS5 and UFS6. Over Europe, the STRIPES index is roughly consistent over time, with UFS5 and UFS6 both underpredicting the magnitude. Like the North Atlantic, there is no noticeable change between UFS5 and UFS6 over this region.

d. MJO teleconnections to the Northern Hemisphere storm tracks

One of the hallmark features of large-scale circulation variability is over the storm track regions. The extratropical cyclone activity in weeks 3-4 of the forecasts of the two UFS prototypes and ERA-I are shown in Fig. 13 as composites of the MJO phases 8-1, 2-3, 4-5, and 6-7 at the initial time of the forecasts. We focus on phases 4-5 and 6-7 when the teleconnection signal is more significant in ERA-I. For phases 4-5 (Fig. 13g-i), both prototypes capture the strong anomalies in the extratropical cyclone activity over the North Pacific. The east-west dipole pattern over the North Pacific is better captured by UFS6, while the spatial patterns in UFS5 display a north-south shift of the storm track. The weakening of the storm track over the North America and North Atlantic seen in ERA-I is captured by both prototypes; however, they predict enhanced extratropical cyclone activity over southeast US, which is not consistent with the ERA-I. For phases 6-7 (Fig. 13j-l), there is an east-west dipole pattern of the storm track over the North Pacific in ERA-I, and both prototypes simulate this east-west dipole pattern. However, the dipole pattern is shifted further eastward in UFS5, while UFS6 captures the pattern over a location that is more consistent with ERA-I. Both prototypes also capture the north-south dipole pattern over the North Atlantic.

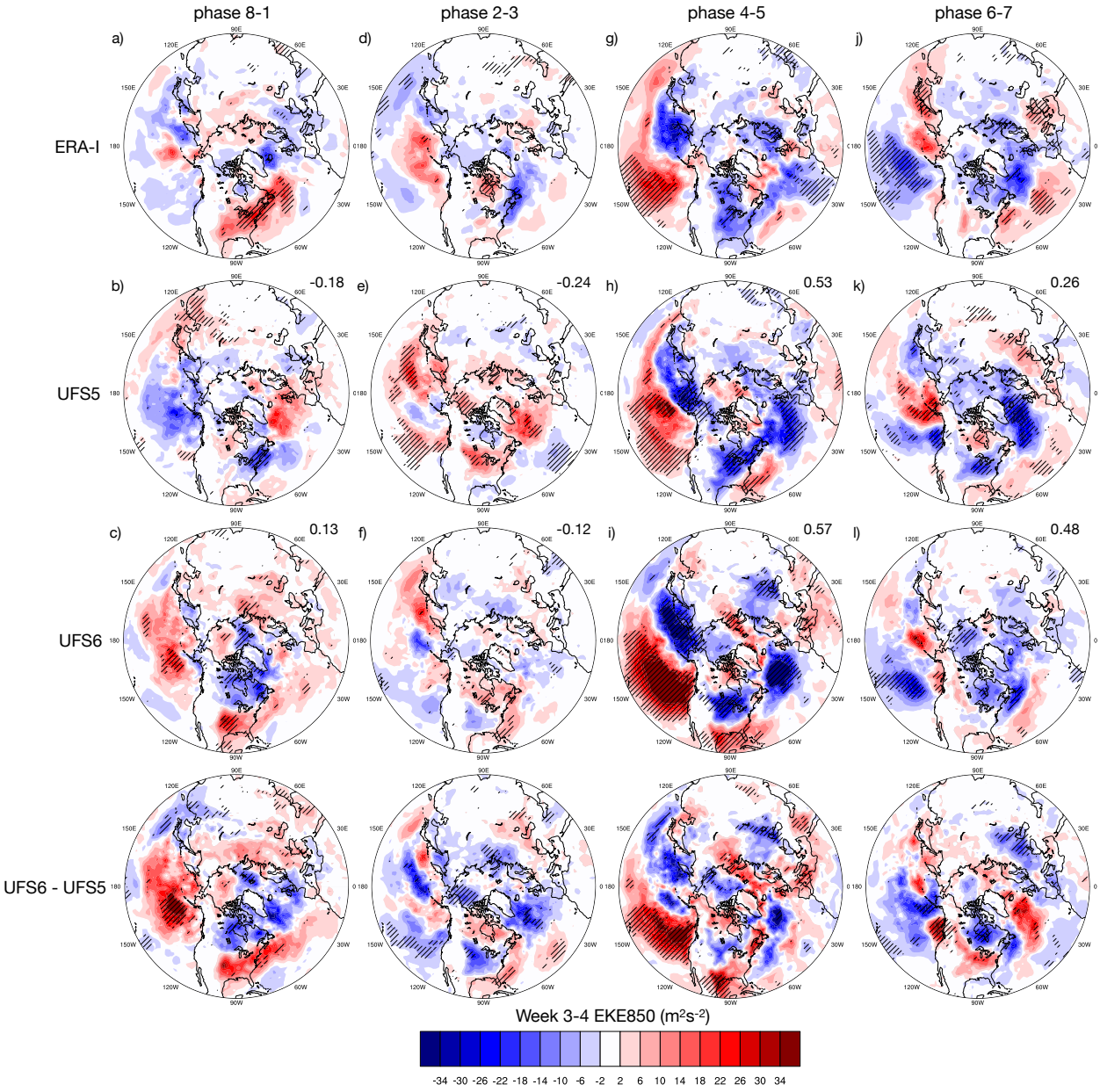

Fig. 13 Composites of week 3-4 extratropical cyclone activity (EKE850) when MJO is in phases 8-1 (a-c), 2-3 (d-f), 4-5 (g-i) and 6-7 (j-l) at reforecast initialization time. The first row shows the composites of ERA-I, while the second, third, and fourth rows show the composites of UFS5, UFS6, and differences between UFS5 and UFS6, respectively. Hashing represents regions where anomalies are statistically significant at the 0.05 level based on a bootstrap resampling calculation. Pattern correlation between prototypes and ERA-I over the northern hemisphere (20°-80°N) is shown in the upper right corner of each panel for UFS5 and UFS6.

As discussed in Stan et al. (2022), models that better capture the MJO teleconnections of the large-scale circulation (Z500) also better capture the MJO teleconnections of the storm track, due to the fact that the interaction between the storm track and the large-scale circulation is symbiotic in nature (e.g. Cai and Mak 1990). The spatial pattern correlation between prototypes and ERA-I for extratropical cyclone activity and Z500 over the North Atlantic (20°-80°N, 90°W-30°E), the North Pacific and North America (20°-80°N, 120°E-90°W), and the northern hemisphere (20°-80°N) is summarized in Fig. 14. Consistent with the discussion above, across different MJO phases, the teleconnection to the storm track is better captured (e.g., phases 4-5, 6-7) when the teleconnection of Z500 is also better predicted. The pattern correlation is near zero or negative for MJO phases 8-1 and 2-3, partially due to the fact that MJO teleconnections in both large-scale circulation (section 3c) and the storm track are weak in ERA-I. These MJO phases are only shown for the completeness of storm track analysis. For phases 4-5 and 6-7, the pattern correlation is higher in UFS5 than UFS6 over the North Atlantic (Fig. 14a); however, the pattern correlation over the North Pacific and North America is higher in UFS6 than in UFS5. Over the Northern Hemisphere (Fig. 14c), the two prototypes have very similar pattern correlation for the MJO phases 4-5, while UFS6 has a higher pattern correlation in extratropical cyclone activity than UFS5 for phases 6-7.

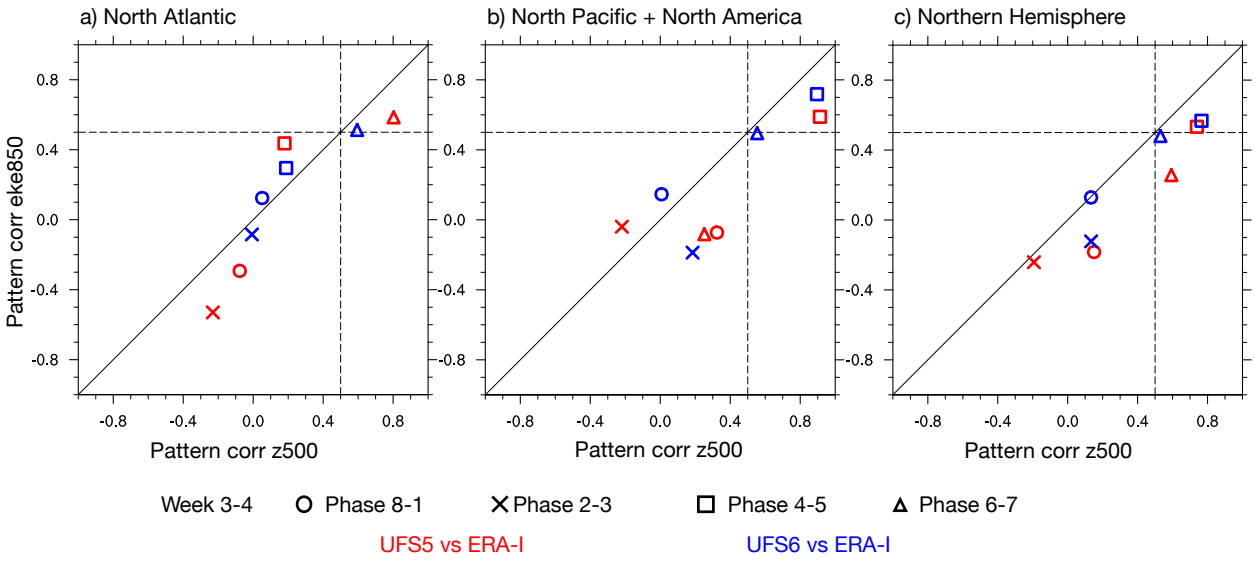

Fig. 14 Pattern correlation of week 3-4 composites of EKE850 (y-axis) and Z500 (x-axis) between ERA-I and UFS5 (red) or UFS6 (blue) over the North Atlantic (20°-80°N, 90°W-30°E), the North Pacific and North America (20°-80°N, 120°E-90°W), and the Northern Hemisphere (20°-80°N). Different symbols represent different MJO phases. The solid line shows the 1:1 line. The dashed lines represent 0.5 pattern correlation coefficient.

e. MJO teleconnections to the Northern Hemisphere 2-meter temperature distribution

Next, we focus on how the prototypes predict the MJO-induced T2m teleconnections over the Northern Hemisphere. In ERA-I, the MJO phase 3 is followed 3-4 weeks later by a cold anomaly over the Arctic region, while subpolar regions show a warm anomaly (Fig. 15). Both prototypes forecast the sign, amplitude, and approximate locations of temperature anomalies seen in ERA-I. In both prototypes, the pattern correlation for each of the two weeks is smaller than in any of the models in the S2S database (Stan et al. 2022). Over Northern America, UFS5 does not maintain the persistence of the pattern from week 3 to week 4. UFS6 maintains the patterns over North America but not over East Asia or Europe.

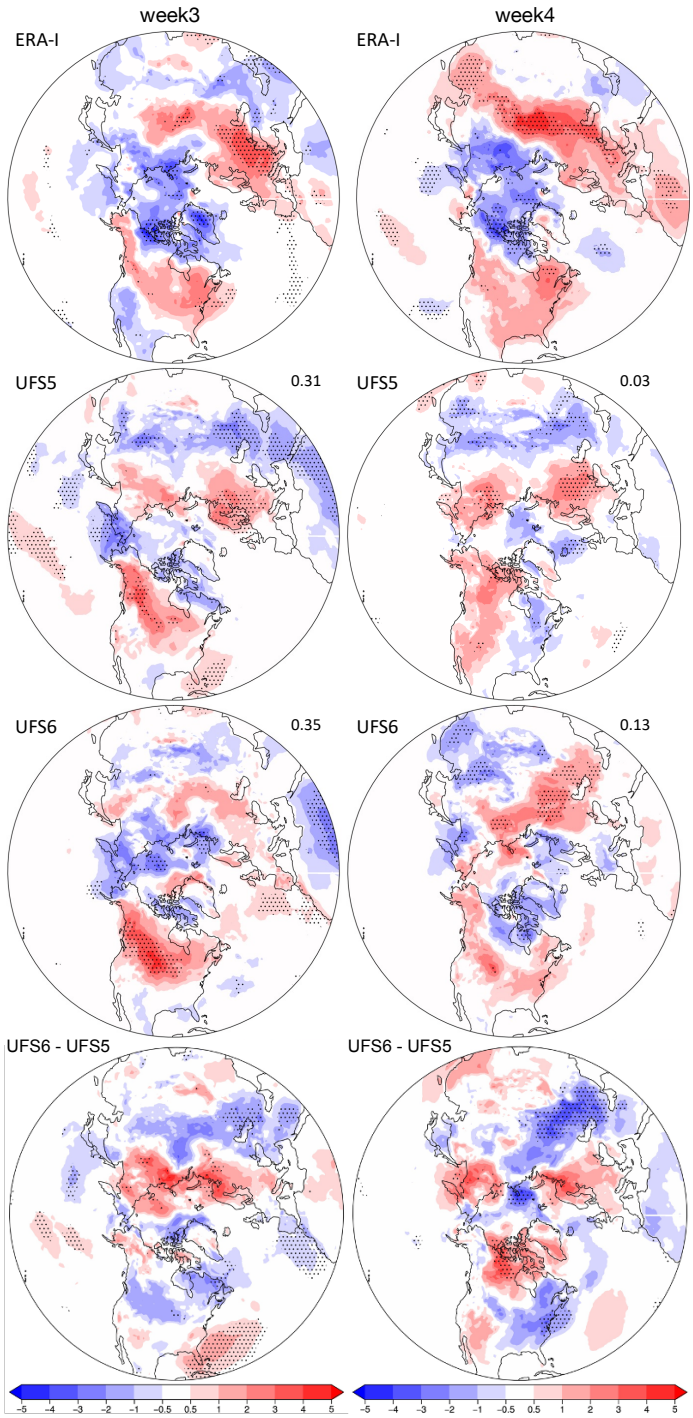

596

597 **Fig. 15** Composites of T2m anomaly in week 3 (left column) and 4 (right column) after the MJO phase 3
598 in ERA-I, UFS5, and UFS6, as well as differences between UFS6 and UFS5. Dotted areas denote anomalies
599 statistically significant at the 0.05 level based on a bootstrap resampling calculation. Numbers in the upper
600 right corners show the pattern correlation between reforecasts and ERA-I.

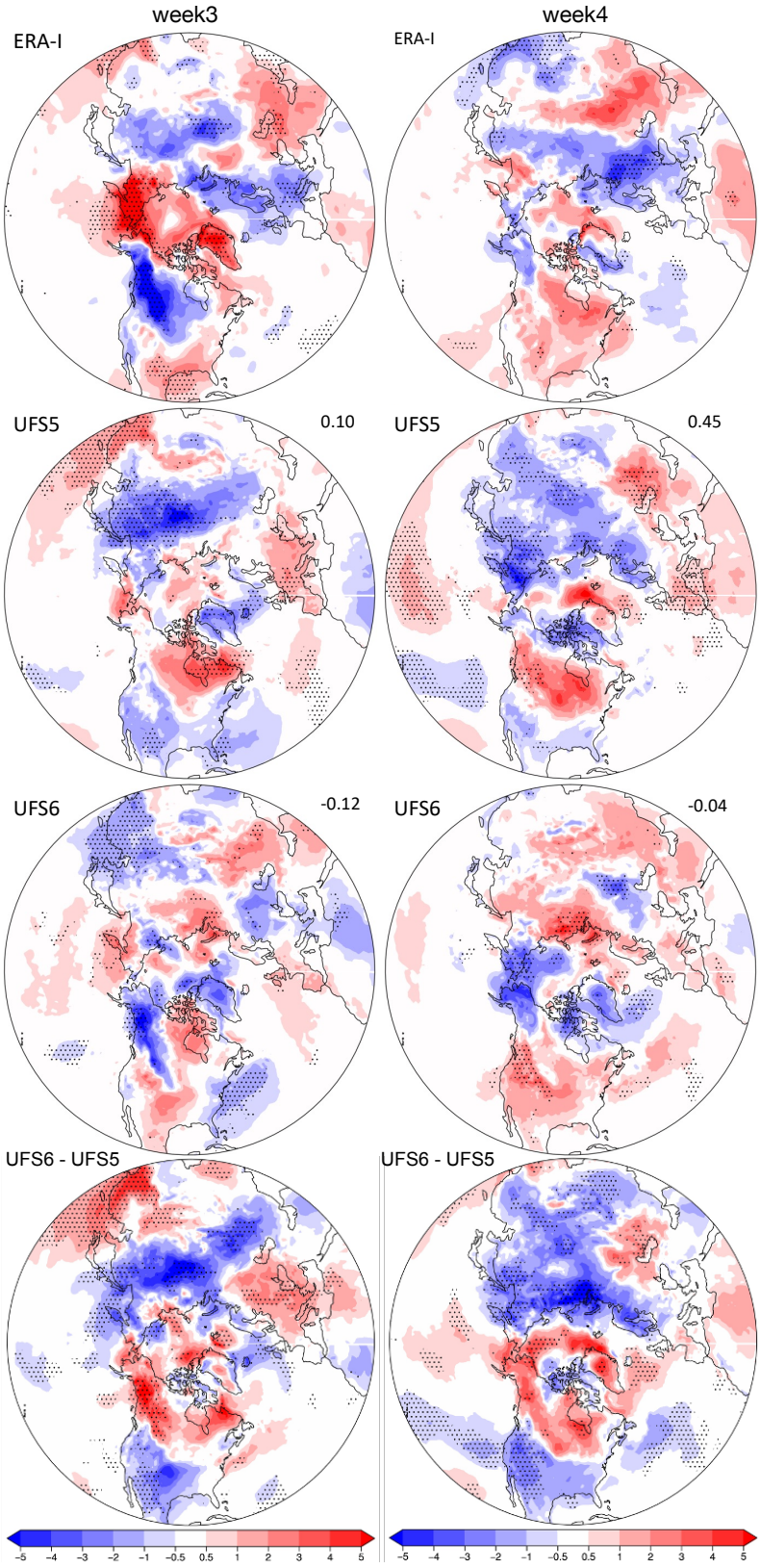

601

602 **Fig. 16** The same as Fig. 15, but for the MJO phase 7.

For the MJO phase 7 (Fig. 16), the sign of the T2m anomaly over North America reverses from week 3 to week 4. Both prototypes struggle to capture this reversal of sign displayed by ERA-I. The cold anomaly over Eurasia is more or less captured by UFS5 but not by UFS6, which is likely the reason why UFS5 has higher pattern correlation in week 4 than UFS6.

f. MJO teleconnections to Northern Hemisphere precipitation

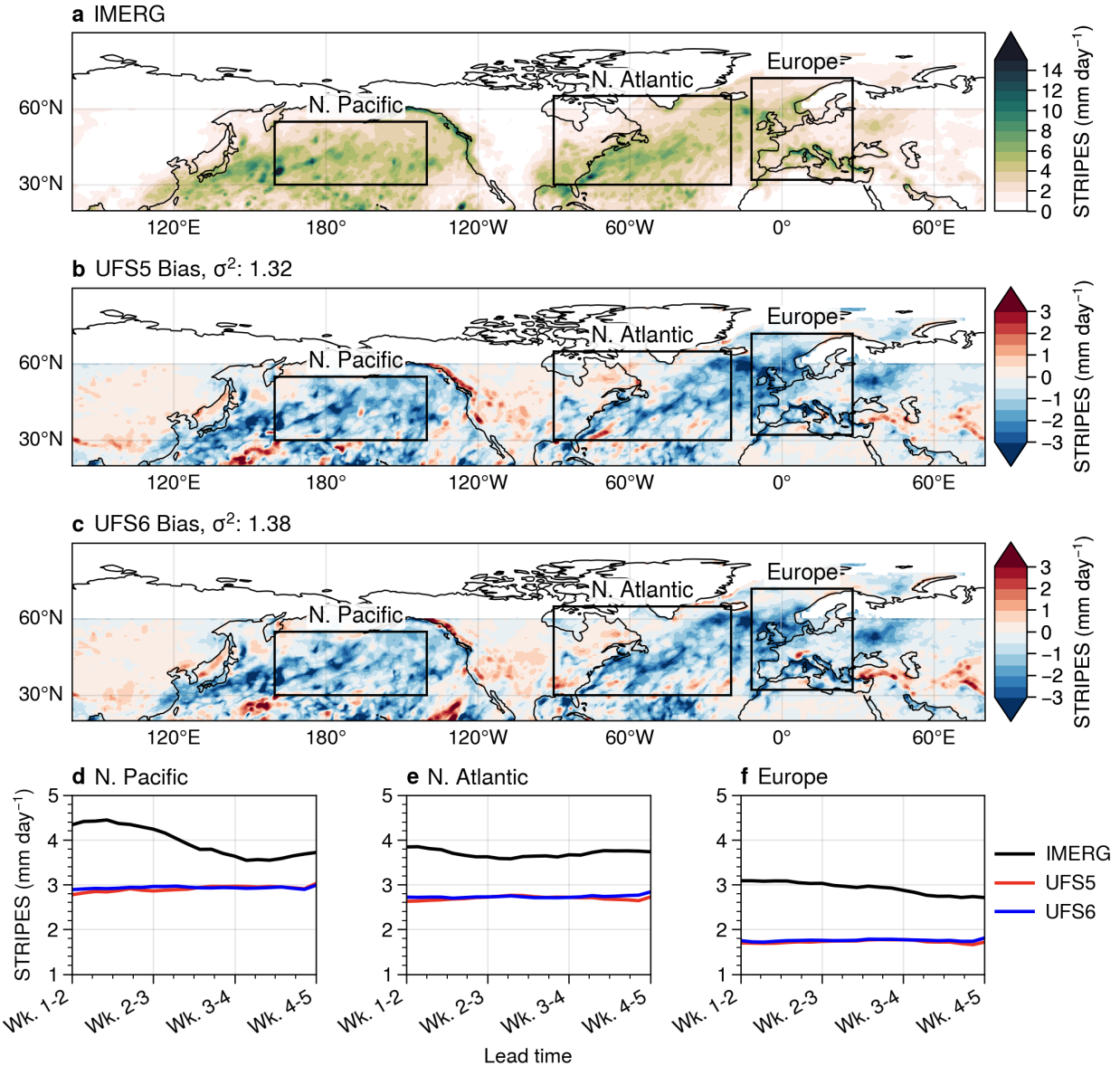

Fig. 17 As in Fig. 12, but for precipitation.

611

612 STRIPES indices for observed precipitation are shown in Fig. 16a. Large values are present
613 over the storm tracks, over the central west coast of North America, over the southeastern US, and
614 around the coasts of Europe. Errors in the forecast STRIPES index for UFS5 and UFS6 are shown
615 in Fig. 17b-c, respectively. Despite a positive climatological error in precipitation (Fig. S5),
616 interestingly the STRIPES error is negative throughout most of the Northern Hemisphere. An
617 exception to this pattern is present over North America, especially the central west, where the error
618 is positive. The Northern Hemisphere (20°-90° N) variance of the STRIPES bias for precipitation
619 is somewhat increased from 1.32 to 1.38 $(\text{mm day}^{-1})^2$ between UFS5 and UFS6.

620 Next, we inspect the temporal evolution of the STRIPES index for precipitation for
621 different regions. Fig. 17d-f shows the time series of the STRIPES index from observations, UFS5,
622 and UFS6 computed using overlapping 2-week windows over the North Pacific, North Atlantic,
623 and Europe. The magnitude is underpredicted by about 1.5 mm day^{-1} for all regions, and unchanged
624 between UFS5 to UFS6. This is consistent with a similar underestimation of the magnitude of the
625 STRIPES index for Z500 by both prototypes (section 3c). The MJO modulates extratropical
626 precipitation via teleconnection of large-scale circulation (e.g., Z500). Thus, it is not surprising
627 that UFS5 and UFS6 underestimate the precipitation variability associated with the MJO
628 (STRIPES index of precipitation; Fig. 17), since the MJO-related variability of large-scale
629 circulation (STRIPES index of Z500; Fig. 12) is also underestimated.

630

631 **4. Summary and Discussion**

632 Two versions of the UFS model, referred to as prototype 5 (here, UFS5) and 6 (UFS6),
633 have been evaluated and compared to determine their ability to forecast the climatology of
634 tropospheric basic states, the MJO, and its extratropical teleconnections. The comparison was

motivated by the different vertical resolutions (more layers in UFS6) and location of model top (higher top in UFS6) in the atmospheric component of the two prototypes. A caveat of the study is that UFS6 also has other updates in the physics parameterizations and due to the nature of the model data the relative impacts of physics and grid changes cannot be disentangled. Because the vertical resolution is roughly doubled the implicit assumption is that the observed differences are related to the changes in the vertical grid rather than the minor updates in the physics parameterizations. Since model physics is sensitive to model vertical resolution as discussed in section 2, in practice a clean comparison with identical model physics and different model vertical resolution is currently not reasonable. The two prototypes share the same ocean, sea ice, wave, and land model components.

The two prototypes display similar biases in the tropospheric basic state and prediction skill in Z500, T2m, extratropical cyclones, and precipitation. In terms of the prediction of the MJO, UFS5 skill is slightly higher after week 3 compared to UFS6, but not comparable to most recent forecast models (e.g., Kim et al. 2018 and Kim et al. 2019). Both models also have large biases in predicting the eastward propagation of the MJO especially over the MC. The MC barrier effect is often exaggerated in both forecasting and climate models, making it one of the major deficiencies in predicting the MJO. The reasons for this bias are complex and beyond the scope of this study

The pattern and amplitude of large-scale circulation (Z500) teleconnections are slightly better captured by UFS6 compared with UFS5. The two prototypes show similar biases in capturing the MJO-related variability of Z500 over the North Atlantic and Europe, while UFS6 has smaller biases over the North Pacific region than UFS5. This improvement in UFS6 is consistent with the results from pattern CC and the relative amplitude of Z500 over the PNA

region, which is possibly due to a better representation of the waveguide over the North Pacific in UFS6. This is similar to Vitart et al. (2022), who attributed the errors in the MJO teleconnection in the ECMWF IFS model to the biases in the upper troposphere large-scale circulation over the central North Pacific. Despite the improvement in UFS6, both UFS5 and UFS6 underestimate the MJO-related variability of the large-scale circulation over the North Atlantic, the North Pacific and Europe.

Similarly, the precipitation variability associated with the MJO is also underestimated and unchanged between both prototypes.

For weeks 3-4 extratropical cyclone activity, the two prototypes capture the MJO-associated signal in RMM phases 6-7 over the North Atlantic (consistent with S2S models; Stan et al. 2022), and phases 4-5 over the North Pacific and North America (further discussion below). As the variability of extratropical cyclone activity is highly modulated by the large-scale circulation, the MJO-related extratropical cyclone activity signal is better captured by the two prototypes when the MJO-related large-scale circulation is well predicted, consistent with Stan et al. (2022). For weeks 3-4 T2m, both prototypes forecast the sign and approximate locations of temperature anomalies over the mid-to-high latitude continents for RMM phase 3. For phase 7, both prototypes fail to capture the sign reversal over North America from week 3 to 4 in the ERA-I, while cold anomalies over Eurasia are better captured by UFS5 than UFS6, which likely results in higher T2m pattern correlation in UFS5.

		Comparison
MJO	RMM index	ACC in week 3 is higher for UFS5thanfor UFS6. UFS5 and UFS6 show similar biases in MJO propagation speed and amplitude.

MJO teleconnections	Z500	Pattern CC and relative amplitude	UFS6 compares better to observations than UFS5
		STRIPES index	UFS6 has reduced errors over the Northwest Pacific. Elsewhere, UFS5 and UFS6 show similar performance.
	T2m	Pattern Correlation	UFS6 has a slightly higher pattern correlation value after the MJO phase 3 than UFS5 and a lower value after the MJO phase 7, especially in week 4.
	Extratropical cyclone activity	Pattern Correlation	UFS5 and UFS6 show similar performance.
	Precipitation	STRIPES index	UFS5 and UFS6 show similar performance.

Table. 2 Model performance in predicting the MJO and MJO-teleconnection.

Overall, the two prototypes show a similar performance in predicting the tropospheric basic states and weekly variability including the MJO and its teleconnections. The major findings are summarized in Table 2. UFS6 shows a slight improvement from UFS5 in capturing the MJO-related large-scale circulation over the North Pacific. We thus conclude that the increase in vertical levels and the upgrades in model physics only show limited benefits in predicting the MJO teleconnections through the tropospheric pathway. As the MJO teleconnections are driven by the Rossby waves induced by the MJO, differences in the simulated teleconnections can be due to differences in the MJO itself and/or the extratropical tropospheric basic state. While the increase in vertical resolution and model top yields statistically significant differences between the tropospheric basic state, these differences do not translate into robust improved predictions of the MJO and MJO teleconnections in the UFS model. This result suggests that the vertical resolution is not the main reason for the model deficiencies in representing the MJO

691 teleconnection in the troposphere (with model physics and horizontal resolution in the current
692 UFS framework; not necessarily for other prediction models) Whether this is also true for the
693 stratospheric pathway will be analyzed in Part II.

694 With limited reforecast samples (one ensemble member, 2011-2018), it is difficult to
695 compare UFS with other S2S models, which usually have longer reforecast periods and multiple
696 ensemble members. In general, the spatial patterns in composites of Z500, T2m and extratropical
697 cyclone activity teleconnection for UFS5 and UFS6 look similar to that of other S2S models
698 (e.g., in Stan et al. 2022). UFS skill in pattern CC over the PNA region (Fig. 11), which is less
699 dependent on the number of reforecasts, drops below 0.5 at around day 8 or 9. This is less
700 skillful than the top-performing S2S model, and is close to the lower end of the performance of
701 the S2S models (Stan et al. 2022).

702 These results come with several caveats. As the reforecast period (2011-2018) is
703 relatively short, the number of reforecasts initialized in particular MJO phases is even smaller,
704 meaning that the MJO teleconnection composites could be dominated by noise and/or low
705 frequency variability. For example, the EKE850 composites of phases 4-5 have much stronger
706 amplitude than that of the opposite MJO phases (8-1), partially due to the fact that only 6
707 reforecasts are initialized in MJO phases 4-5 (Fig. 13), while 11 reforecasts are initialized in
708 phases 8-1. Phases 4-5 EKE850 composite maps look similar to those in previous studies (e.g.,
709 Stan et al. 2022), and the spatial correlation between UFS and ERA-I is high over the North
710 Pacific and North America region (Fig. 13). However, the MJO may not be the sole contributor
711 to the teleconnection patterns as El Niño Southern Oscillation (ENSO) may also play a role,
712 considering ENSO could modulate the MJO teleconnection (Moon et al. 2011; R. Lee et al.
713 2019; Arcodia and Kirtman 2023).

Three of the six reforecasts initialized in MJO phases 4-5 are within the 2015-16 winter, a strong El Niño event. El Niño may induce an eastward extension of the North Pacific storm track (e.g., Chang et al. 2002; Eichler and Higgins 2006) which is similar to the weeks 3-4 composites of the MJO phases 4-5. As it takes 1-2 weeks for the MJO-induced Rossby waves to reach the extratropics, the weeks 3-4 MJO teleconnection over the North Pacific in phases 4-5 (which exhibit enhanced convective anomalies over the MC and the western Pacific) is probably triggered by the MJO convective anomalies over the central and eastern Pacific. These anomalies coincide with El Niño-driven tropical convective anomalies as the MJO propagates eastward. Thus, the MJO phases 4-5 composite (Fig. 13) is likely a mixture of both MJO and ENSO teleconnections. In fact, weeks 1-2 composites of MJO phases 4-5 (not shown) also display very similar spatial patterns at weeks 3-4 over the North Pacific, suggesting that these anomalies are driven by low-frequency variability such as ENSO rather than subseasonal variability such as the MJO. The high spatial correlation between UFS and ERA-I phases 4-5 composite may not necessarily reflect that UFS is capturing the MJO phases 4-5 teleconnection well, but rather that UFS is capturing the ENSO teleconnection well. Reforecasts covering longer time periods are required to isolate the MJO teleconnection from other variability.

The impact of vertical resolution on the model biases and subseasonal forecast skill is not documented in the literature and an in-depth analysis is beyond the scope of this study. Part II will consider in more detail the role of the stratosphere for the surface response, and in particular anomalies over Eurasia.

Acknowledgements

This study was supported by the NOAA/OAR Weather Program Office through grant NA22OAR4590216. H. Kim was also supported by the NOAA grant NA22OAR4590168. Support from the Swiss National Science Foundation through project PP00P2_198896 to D.D. is gratefully acknowledged. We thank two anonymous reviewers for their constructive comments that improved the clarity of the manuscript.

References

Adcroft, A., Anderson, W., Balaji, V., Blanton, C., Bushuk, M., Dufour, C. O., et al. (2019). The GFDL global ocean and sea ice model OM4.0: Model description and simulation features. Journal of Advances in Modeling Earth Systems, 11, 3167–3211. https://doi.org/10.1029/2019MS001726

Arcodia, M.C., Kirtman, B.P. Using simplified linear and nonlinear models to assess ENSO-modulated MJO teleconnections. Clim Dyn 61, 5443–5463 (2023). https://doi.org/10.1007/s00382-023-06864-x

Barnes, E. A., S. M. Samarasinghe, I. Ebert-Uphoff, and J. C. Furtado, 2019: Tropospheric and stratospheric causal pathways between the MJO and NAO. J. Geophys. Res., 124, 9356–9371, https://doi.org/10.1029/2019JD031024.

Bauer, P., Beljaars, A., Ahlgrimm, M., Bechtold, P., Bidlot, J.-R., Bonavita, M., Bozzo, A., Forbes, R., Hólm, E., Leutbecher, M., Lopez, P., Magnusson, L., Prates, F., Rodwell, M., Sandu, I., Untch, A., & Vitart, F. (2013). Model cycle 38r2: Components and performance (704): ECMWF Technical Memoranda. 58 Retrieved from https://www.ecmwf.int/node/7986, https://doi.org/10.21957/xc1r0lj6l

759 Butler, A. H., Arribas, A., Athanassiadou, M., Baehr, J., Calvo, N., Charlton-Perez, A.,
760 Déqué, M., Domeisen, D. I. V., Fröhlich, K., Hendon, H., Imada, Y., Ishii, M., Iza, M.,
761 Karpechko, A. Y., Kumar, A., MacLachlan, C., Merryfield, W. J., Müller, W. A.,
762 O'Neill, A., Scaife, A. A., Scinocca, J., Sigmond, M., Stockdale, T. N., & Yasuda, T.
763 (2016). The Climate-system Historical Forecast Project: Do stratosphere-resolving
764 models make better seasonal climate predictions in boreal winter? Quarterly Journal of
765 the Royal Meteorological Society, 142(696), 1413–1427. https://doi.org/10.1002/qj.2743
766 Cai, Z., K. Wei , L. Xu , X. Lan , W. Chen , and D. Nath , 2017: The influences of model
767 configuration on the simulations of stratospheric Northern-Hemisphere polar vortex in
768 the CMIP5 models. Adv. Meteor., 2017, 7326759, https://doi.org/10.1155/2017/7326759.
769 Chang, E. K. M., S. Lee, and K. L. Swanson, 2002: Storm Track Dynamics. J. Climate, 15,
770 2163–2183, https://doi.org/10.1175/1520-0442(2002)015<02163:STD>2.0.CO;2.
771 Charlton-Perez, A. J., and Coauthors, 2013: On the lack of stratospheric dynamical variability in
772 low-top versions of the CMIP models. *J. Geophys. Res., Atmos.*, **118**, 2494-2505.
773 doi:10.1002/jgrd.50125
774 Chandran, A., Collins, R. L., & Harvey, V. L., 2014: Stratosphere-mesosphere coupling during
775 stratospheric sudden warming events. Advances in Space Research, 53(9), 1265–1289.
776 https://doi.org/10.1016/j.asr.2014.02.005
777 Dee, D. P., and Coauthors, 2011: The ERA-Interim reanalysis: Configuration and performance
778 of the data assimilation system. Quart. J. Roy. Meteor. Soc., 137, 553–597,
779 https://doi.org/10.1002/qj.828.

780 Domeisen, D. I. V., and Coauthors, 2020a: The role of stratosphere in subseasonal to seasonal
781 prediction: 1. Predictability of the stratosphere. *J. Geophys. Res.*, **125**, e2019JD030920.
782 doi:10.1029/2019JD030920
783 Domeisen, D. I., Butler, A. H., Charlton-Perez, A. J., Ayarzagüena, B., Baldwin, M. P., Dunn-
784 Sigouin, E. et al. 2020b: The role of the stratosphere in subseasonal to seasonal
785 prediction: 2. Predictability arising from stratosphere-troposphere coupling. J. Geophys.
786 Res., 125, e2019JD030923. https://doi.org/10.1029/2019JD030923
787 Eichler, T., and W. Higgins, 2006: Climatology and ENSO-Related Variability of North
788 American Extratropical Cyclone Activity. J. Climate, 19, 2076–2093,
789 https://doi.org/10.1175/JCLI3725.1.
790 Feng, P.-N., H. Lin, J. Derome, and T. Merlis, 2021: Forecast skill of the NAO in the
791 subseasonal-to-seasonal prediction models. *J. Climate*, **34**, 4757-4769. doi:10.1175/JCLI-
792 D-20-0430.1
793 Ferranti, L., Palmer, T. N., Molteni, F., & Klinker, E. (1990). Tropical-extratropical interaction
794 associated with the 30–60 day oscillation and its impact on medium and extended range
795 prediction. Journal of the Atmospheric Sciences, 47, 2177–2199.
796 Gottschalck, J., and Coauthors, 2010: A Framework for Assessing Operational Madden–Julian
797 Oscillation Forecasts. Bull. Amer. Meteor. Soc., 91, 1247–1258,
798 https://doi.org/10.1175/2010BAMS2816.1.
799 Garfinkel, C. I., W. Chen, Y. Li, C. Schwartz, P. Yadav, and D. Domeisen, 2022: The Winter
800 North Pacific Teleconnection in Response to ENSO and the MJO in Operational
801 Subseasonal Forecasting Models Is Too Weak. J. Climate, 35, 8013–8030,
802 https://doi.org/10.1175/JCLI-D-22-0179.1.

803 Harris, L. M., and S.-J. Lin, 2013: A two-way nested global-regional dynamical core on the
804 cubed-sphere grid. Mon. Wea. Rev., 141, 283–306, https://doi.org/10.1175/MWR-D-11-
805 00201.1.
806 Henderson, S. A., E. D. Maloney, and S. Son, 2017: Madden–Julian Oscillation Pacific
807 Teleconnections: The Impact of the Basic State and MJO Representation in General
808 Circulation Models. J. Climate, 30, 4567–4587, https://doi.org/10.1175/JCLI-D-16-
809 0789.1.
810 Hoskins, B. J., and T. Ambrizzi, 1993: Rossby Wave Propagation on a Realistic Longitudinally
811 Varying Flow. J. Atmos. Sci., 50, 1661–1671, https://doi.org/10.1175/1520-
812 0469(1993)050<1661:RWPOAR>2.0.CO;2.
813 Huffman, G. J., D. T. Bolvin, D. Braithwaite, K. Hsu, R. Joyce, C. Kidd, E. J. Nelkin, and P.
814 Xie, 2015: NASA Global Precipitation Measurement (GPM) Integrated Multi-Satellite
815 Retrievals for GPM (IMERG). NASA/GSFC Algorithm Theoretical Basis Doc., 30pp.
816 Jenney, A. M., Randall, D. A., & Barnes, E. A. (2019). Quantifying regional sensitivities to
817 periodic events: Application to the MJO. Journal of Geophysical Research: Atmospheres,
818 124, 3671– 3683. https://doi.org/10.1029/2018JD029457
819 Jiang, Z., S. B. Feldstein, and S. Lee, 2017: The relationship between the Madden–Julian
820 Oscillation and the North Atlantic Oscillation. Quart. J. Roy. Meteor. Soc., 143, 240–250,
821 https://doi.org/10.1002/qj.2917.
822 Karoly, D., 1983: Rossby wave propagation in a barotropic atmosphere. Dyn. Atmos. Oceans, 7,
823 111–125, https://doi.org/10.1016/0377-0265(83)90013-1.
824 Kim, H., F. Vitart, and D. E. Waliser, 2018: Prediction of the Madden–Julian Oscillation: A
825 Review. J. Climate, 31, 9425–9443, https://doi.org/10.1175/JCLI-D-18-0210.1.

826 Kim, H., Janiga, M. A., & Pegion, K. (2019). MJO propagation processes and mean biases in the
827 SubX and S2S reforecasts. Journal of Geophysical Research: Atmospheres, 124, 9314–
828 9331. https://doi.org/10.1029/2019JD031139
829 Lawrence, Z. D., Abalos, M., Ayarzagüena, B., Barriopedro, D., Butler, A. H., Calvo, N., de la
830 Cámara, A., Charlton-Perez, A., Domeisen, D. I. V., Dunn-Sigouin, E., García-Serrano,
831 J., Garfinkel, C. I., Hindley, N. P., Jia, L., Jucker, M., Karpechko, A. Y., Kim, H., Lang,
832 A. L., Lee, S. H., Lin, P., Osman, M., Palmeiro, F. M., Perlwitz, J., Polichtchouk, I.,
833 Richter, J. H., Schwartz, C., Son, S.-W., Statnaia, I., Taguchi, M., Tyrrell, N. L., Wright,
834 C. J., and Wu, R. W.-Y, 2022: Quantifying stratospheric biases and identifying their
835 potential sources in subseasonal forecast systems, Weather Clim. Dynam., 3, 977–1001,
836 https://doi.org/10.5194/wcd-3-977-2022
837 Lee, R. W., Woolnough, S. J., Charlton-Perez, A. J., & Vitart, F. (2019). ENSO modulation of
838 MJO teleconnections to the North Atlantic and Europe. Geophysical Research Letters,
839 46, 13535–13545. https://doi.org/10.1029/2019GL084683
840 Lee, E., E. Lee, and I. Choi, (2019): Impact of Increased Vertical Resolution on Medium-Range
841 Forecasts in a Global Atmospheric Model. Mon. Wea. Rev., 147, 4091–4106,
842 https://doi.org/10.1175/MWR-D-18-0387.1.
843 Liebmann, B., and C. A. Smith, 1996: Description of a complete (interpolated) outgoing
844 longwave radiation dataset. Bull. Amer. Meteor. Soc., 77, 1275–1277,
845 https://doi.org/10.1175/1520-0477-77.6.1274.
846 Madden, R. A., and P. R. Julian, 1971: Detection of a 40-50 day oscillation in the zonal wind in
847 the tropical Pacific. *J. Atmos. Sci.*, **28**, 702-708. doi:10.1175/1520-
848 0469(1971)<0702:DOADOI>2.0.CO;2

Madden, R. A., and P. R. Julian, 1972: Description of global-scale circulation cells in the tropics with a 40-50 day period. *J. Atmos. Sci.*, **29**, 1109-1123. doi:10.1175/1520-0469(1972)029<1109:DOGSCC>2.0.CO;2

Mariotti, A., and Coauthors, 2020: Windows of Opportunity for Skillful Forecasts Subseasonal to Seasonal and Beyond. Bull. Amer. Meteor. Soc., 101, E608–E625, https://doi.org/10.1175/BAMS-D-18-0326.1.

Matthews, A. J., B. J. Hoskins, and M. Masutani, 2004: The global response to tropical heating in the Madden–Julian oscillation during the northern winter. Quart. J. Roy. Meteor. Soc., 130, 1991–2011, https://doi.org/10.1256/qj.02.123.

McTaggart-Cowan, R., Vaillancourt, P. A., Zadra, A., Chamberland, S., Charron, M., Corvec, S., et al. (2019). Modernization of atmospheric physics parameterization in Canadian NWP. Journal of Advances in Modeling Earth Systems, 11, 3593–3635. https://doi.org/10.1029/2019MS001781

Moon, JY., Wang, B. & Ha, KJ. ENSO regulation of MJO teleconnection. Clim Dyn 37, 1133–1149 (2011). https://doi.org/10.1007/s00382-010-0902-3

Mori, M., & Watanabe, M. (2008). The growth and triggering mechanisms of the PNA: A MJO-PNA coherence. Journal of the Meteorological Society of Japan, 86, 213–236.

National Centers for Environmental Prediction, 2019: The Global Forecast System (GFS)—Global Spectral Model (GSM). NOAA, accessed 25 July 2023, https://www.emc.ncep.noaa.gov/emc/pages/numerical_forecast_systems/gfs/documentation.php.

870 Pfahl, S., Schwierz, C., Croci-Maspoli, M., Grams, C. M., & Wernli, H. (2015). Importance of
871 latent heat release in ascending air streams for atmospheric blocking. Nature Geoscience,
872 8(8), 610–614. https://doi.org/10.1038/ngeo2487
873 Putman, W. M., and S.-J. Lin, 2007: Finite-volume transport on various cubed-sphere grids. J.
874 Comput. Phys., 227, 55–78, https://doi.org/10.1016/j.jcp.2007.07.022.
875 Rashid, H. A., H. H. Hendon, M. C. Wheeler, and O. Alves, 2011: Prediction of the Madden–
876 Julian oscillation with the POAMA dynamical prediction system. Climate Dyn., 36, 649–
877 661, doi:10.1007/s00382-010-0754-x.
878 Richter, J. H., and Coauthors, 2020: Subseasonal Prediction with and without a Well-
879 Represented Stratosphere in CESM1. Wea. Forecasting, 35, 2589–2602,
880 https://doi.org/10.1175/WAF-D-20-0029.1.
881 Riddle, E. E., M. B. Stoner, N. C. Johnson, M. L. L'Heureux, D. C. Collins, and S. B. Feldstein,
882 2013: The impact of the MJO on clusters of wintertime circulation anomalies over the
883 North American region. Climate Dyn., 40, 1749–1766, https://doi.org/10.1007/s00382-
884 012-1493-y.
885 Saha, S., and Coauthors, 2014: The NCEP Climate Forecast System Version 2. J. Climate, 27,
886 2185–2208, https://doi.org/10.1175/JCLI-D-12-00823.1.
887 Schwartz, C., & Garfinkel, C. I. (2017). Relative roles of the MJO and stratospheric variability in
888 North Atlantic and European winter climate. Journal of Geophysical Research:
889 Atmospheres, 122, 4184–4201. https://doi.org/10.1002/2016JD025829
890 Schwartz, Chen, and C. I. Garfinkel, 2020: Troposphere-sttratopshere coupling in subseasonal-
891 to-seasonal models and its importance for a realistic extrattropical response to the

Madden-Julian Oscillation. *J. Geophys. Res. Atmos.*, **125**, e2019JD032043. doi:10.1029/2019JD032043

Seo, K., and S. Son, 2012: The global atmospheric circulation response to tropical diabatic heating associated with the Madden–Julian oscillation during northern winter. J. Atmos. Sci., 69, 79–96, https://doi.org/10.1175/2011JAS3686.1.

Seo, K., and Lee, H. (2017). Mechanisms for a PNA-Like Teleconnection Pattern in Response to the MJO, Journal of the Atmospheric Sciences, 74(6), 1767-1781. https://doi.org/10.1175/JAS-D-16-0343.1

Son, S.-W., Kim, H., Song, K., Kim, S.-W., Martineau, P., Hyun, Y.-K., & Kim, Y. (2020). Extratropical prediction skill of the Subseasonal-to-Seasonal (S2S) prediction models. Journal of Geophysical Research: Atmospheres, 125, e2019JD031273. https://doi.org/10.1029/2019JD031273

Stan, C., D. M. Straus, J. S. Frederiksen, H. Lin, E. D. Maloney, and C. Schumacher, 2017: Review of tropical-extratropical teleconnections on intraseasonal time scales, *Rev. Geophys.*, **55**, 902-937. doi:10.1002/2016RG000538

Stan, C., C. Zheng, E. K.-M. Chang, D. I. V. Domeisen, C. Garfienkel, A. M. Jenney, H. Kim, Y.-K. Lim, H. Lin, A. Robertson, C. Schwartz, F. Vitart, J. Wang, P. Yadav, 2022: Advances in the prediction of MJO-Teleconnections in the S2S forecast systems. *Bull. Amer. Meteorol. Soc.*, **103**, E11427-E1447. doi:10.1175/BAMS-D-21-0130.1

Straus, D. M., Domeisen, D. I. V., Lock, S.-J., Molteni, F., and Yadav, P.: Intrinsic predictability limits arising from Indian Ocean Madden–Julian oscillation (MJO) heating: effects on tropical and extratropical teleconnections, 2023: Weather Clim. Dynam., 4, 1001–1018, https://doi.org/10.5194/wcd-4-1001-2023.

915 Strobach, E. J., 2021: Single column model evaluations of mixing length formulations and
916 constraints for the sa-TKE-EDMF scheme. NOAA/NCEP Office Note 504, 28 pp.,
917 https://doi.org/10.25923/0sv0-4916.
918 Strobach, E. J., 2022: A single-column model evaluation of mixing length formulations and
919 constraints for the sa-TKE-EDMF planetary boundary layer parameterization. Wea.
920 Forecasting, 37, 1805–1828, https://doi.org/10.1175/WAF-D-21-0059.1.
921 Stefanova, L., and co-authors. Description and Results from UFS Coupled Prototypes for Future
922 Global, Ensemble and Seasonal Forecasts at NCEP, 2023. doi:10.25923/knxm-kz26
923 Vitart, F. 2017: Madden—Julian Oscillation prediction and teleconnections in the S2S database.
924 Q.J.R. Meteorol. Soc, 143: 2210-2220. https://doi.org/10.1002/qj.3079
925 Vitart, F., R. Emerton, M. Rodwell, M. Balmaseda, T. Haiden, S. Johnson, L. Magnusson, C.
926 Roberts, and I. Sandu, 2022: Investigating biases in the representation of the Pacific sub-
927 tropical jet stream and associated teleconnections (A UGROW sub-project). ECMWF
928 Technical Memorandum, No. 889, European Center for MEdium range Weather
929 Forecast, Reading, England, 20pp.
930 Wallace, J. M. , G. Lim , and M. L. Blackmon , 1988: Relationship between cyclone tracks,
931 anticyclone tracks and baroclinic waveguides. J. Atmos. Sci. , 45, 439–462,
932 https://doi.org/10.1175/1520-0469(1988)045,0439:RBCTAT.2.0.CO;2.
933 Wang, J. , H. M. Kim , D. Kim , S. A. Henderson , C. Stan , and E. D. Maloney , 2020a: MJO
934 teleconnections over the PNA region in climate models. Part I: Performance- and
935 process-based skill metrics. J. Climate , 33, 1051–1067, https://doi.org/10.1175/JCLI-D-
936 19-0253.1.

Wang, J. , H. M. Kim , D. Kim , S. A. Henderson , C. Stan , and E. D. Maloney, 2020b: MJO teleconnections over the PNA region in climate models. Part II: Impacts of the MJO and basic state. J. Climate , 33, 5081-5101, htttps://doi.org/10.1175/JCLI-D-19-0865.1.

White CJ, Domeisen DIV, Acharya N, Adefisan EA, Anderson ML, Aura S, Balogun AA, Bertram D, Bluhm S, Brayshaw DJ, Browell J, Büeler D, Charlton-Perez A, Chourio X, Christel I, Coelho CaS, Deflorio MJ, Delle Monache L, Di Giuseppe F, García-Solórzano AM, Gibson PB, Goddard L, González Romero C, Graham RJ, Graham RM, Grams CM, Halford A, Huang WTK, Jensen K, Kilavi M, Lawal KA, Lee RW, Macleod D, Manrique-Suñén A, Martins ESPR, Maxwell CJ, Merryfield WJ, Muñoz ÁG, Olaniyan E, Otieno G, Oyedepo JA, Palma L, Pechlivanidis IG, Pons D, Ralph FM, Reis DS, Remenyi TA, Risbey JS, Robertson DJC, Robertson AW, Smith S, Soret A, Sun T, Todd MC, Tozer CR, Vasconcelos FC, Vigo I, Waliser DE, Wetterhall F, Wilson RG, 2022: Advances in the application and utility of subseasonal-to-seasonal predictions. Bull Am Meteorol Soc 103:E1448-E1472

Wicker, W., Polichtchouk, I., & Domeisen, D. I. V. 2023: Increased vertical resolution in the stratosphere reveals role of gravity waves after sudden stratospheric warmings. Weather and Climate Dynamics, 4(1), 81–93. https://doi.org/10.5194/wcd-4-81-2023

Wheeler, M. C. , and H. H. Hendon , 2004: An all-season real-time multivariate MJO index: Development of an index for monitoring and prediction. Mon. Wea. Rev. , 132, 1917–1932, https://doi.org/10.1175/1520-0493(2004)132,1917:AARMMI.2.0.CO;2.

Xie, Y.-B., S.-J. Chen, I.-L. Zhang, and Y.-L. Hung, 1963: A preliminarily statistic and synoptic study about the basic currents over southeastern Asia and the initiation of typhoon (in Chinese). Acta Meteor. Sin., 33, 206–217.

960 Yau, A. M. W. , and E. K. M. Chang , 2020: Finding storm track activity metrics that are highly
961 correlated with weather impacts. Part I: Frameworks for evaluation and accumulated
962 track activity. *J. Climate* , **33**, 10 169–10 186, https://doi.org/10.1175/JCLI-D-20-0393.1
963 Zheng, C., and E. K. M. Chang, 2019: The role of MJO propagation, lifetime, and intensity on
964 modulating the temporal evolution of the MJO extratropical response. J. Geophys. Res.
965 Atmos., 124, 5352–5378, https://doi.org/10.1029/2019JD030258.
966 Zheng, C., and E. Kar-Man Chang, 2020: The Role of Extratropical Background Flow in
967 Modulating the MJO Extratropical Response. J. Climate, 33, 4513–4536,
968 https://doi.org/10.1175/JCLI-D-19-0708.1.
969 Zhou, W. D. Yang, S. P. Xie, et al, 2020: Amplified Madden-Julian oscillation impacts in the
970 Pacific-North America region. Nat. Clim. Change. 10, 654-660,
971 https://doi.org/10.1038/s41558-020-0814-0.
972 Zhou, L., L. Harris, J.-H. Chen, K. Gao, B. Xiang, M. Tong, J. J. Huff, and M. Morin, 2022:
973 Improving global weather prediction in GFDL SHiELD through an upgraded GFDL
974 microphysics scheme. J. Adv. Model. Earth Syst., 14, e2021MS002971,
975 https://doi.org/10.1029/2021MS002971.
976

Statements and Declarations

Funding

This study was supported by the NOAA/OAR Weather Program Office through grant NA22OAR4590216. H. Kim and C. Zheng were also supported by the NOAA grant NA22OAR4590168.

Competing Interests

The authors have no relevant financial or non-financial interests to disclose.

Data Availability Statement

ERA-Interim reanalysis is available in https://www.ecmwf.int/en/forecasts/dataset/ecmwf-reanalysis-interim. UFS reforecast data is available on AWS https://registry.opendata.aws/noaa-ufs-s2s/